

MG-MAMPOSSt: A code to test modifications of gravity with internal kinematics and lensing analyses of galaxy clusters

Lorenzo Pizzuti^{1,*}, Ippocratis D. Saltas² and Luca Amendola³

¹ *Osservatorio Astronomico della Regione Autonoma Valle d'Aosta, Loc. Lignan 39, I-11020, Nus, Italy*

² *CEICO, Institute of Physics of the Czech Academy of Sciences, Na Slovance 2, 182 21 Praha 8, Czechia*

³ *Institute of Theoretical Physics, Philosophenweg 16, Heidelberg University, 69120, Heidelberg, Germany*

Accepted XXX. Received YYY; in original form ZZZ

ABSTRACT

We present an upgraded version of MG-MAMPOSSt, an extension of the MAMPOSSt algorithm that performs Bayesian fits of models of mass and velocity anisotropy profiles to the distribution of tracers in projected phase space, to handle modified gravity models and constrain their parameters. The new version implements two distinct types of gravity modifications, namely general chameleon and Vainshtein screening, and is further equipped with a Monte-Carlo-Markov-Chain module for an efficient parameter space exploration. The program is complemented by the CLUSTERGEN code, capable of producing mock galaxy clusters under the assumption of spherical symmetry, dynamical equilibrium, and Gaussian local velocity distribution functions as in MAMPOSSt. We demonstrate the potential of the method by analysing a set of synthetic, isolated spherically-symmetric dark matter haloes, focusing on the statistical degeneracies between model parameters. Assuming the availability of additional lensing-like information, we forecast the constraints on the modified gravity parameters for the two models presented, as expected from joint lensing+internal kinematics analyses, in view of upcoming galaxy cluster surveys. In Vainshtein screening, we forecast the weak lensing effect through the estimation of the full convergence-shear profile. For chameleon screening, we constrain the allowed region in the space of the two free parameters of the model, further focusing on the $f(\mathcal{R})$ subclass to obtain realistic bounds on the background field $|f_{\mathcal{R}0}|$. Our analysis demonstrates the complementarity of internal kinematics and lensing probes for constraining modified gravity theories, and how the bounds on Vainshtein-screened theories improve through the combination of the two probes.

Key words: dark energy – galaxies: clusters: general – cosmology: miscellaneous

1 Introduction

Galaxy clusters constitute a very useful probe to test gravity theories, offering a rich laboratory to study the physics of dark matter, dark energy and gravity. Combinations of spectroscopic and lensing observations allow for the reconstruction of the cluster’s mass profile, which in turn provide valuable information about the local gravitational potentials Φ and Ψ that appear in the linearly perturbed metric. This idea has formed the basis for a multitude of phenomenological tests for dark energy theories beyond General Relativity (GR). The most popular theoretical frameworks in this context have been scalar-tensor theories, which extend GR through a new dynamical scalar field. Their theory space has seen strong constraints after the recent gravitational wave observations (e.g. Ezquiaga & Zumalacárregui 2017; Creminelli & Vernizzi 2017; Sakstein & Jain 2017; Baker et al. 2017; Dima & Vernizzi 2018; Kobayashi & Hiramatsu 2018; Amendola et al. 2018). The scalar field propagates a new fifth force which modifies the usual Newtonian potential at local scales leaving a phenomenological footprint on the in-

ternal kinematics and lensing of galaxy clusters. The family of scalar-tensor theories includes the conformally-coupled theories such as Brans-Dicke or $f(\mathcal{R})$ gravity, or the more general Horndeski, beyond Horndeski and the recently introduced Degenerate Higher-Order Scalar-Tensor (DHOST hereafter) theories (Zumalacárregui & García-Bellido 2014; Ben Achour et al. 2016; Langlois et al. 2017; Langlois 2019; Kobayashi 2019; Amendola et al. 2020). Previous works have placed strong constraints on $f(\mathcal{R})$ gravity through the abundance of galaxy clusters (Schmidt et al. 2009; Rapetti et al. 2010; Rapetti et al. 2011; Ferraro et al. 2011; Lombriser et al. 2012b; Cataneo et al. 2015, 2016), or combining reconstructions of the cluster’s thermal and lensing mass (Terukina & Yamamoto 2012; Terukina et al. 2014; Wilcox et al. 2015; Sakstein et al. 2016; Salzano et al. 2016, 2017b). What is more, the combination of lensing and internal kinematics reconstruction of a galaxy cluster mass profile can provide a powerful test based on the gravitational slip parameter η , which defines the deviation from Einsteinian gravity. This was pursued by Pizzuti et al. (2016, 2019), who forecasted

galaxy cluster constraints on the gravitational slip following a simple phenomenological approach.

Building on previous works (eg. [Pizzuti et al. 2017](#), hereafter Paper I), here we present the upgraded MG-MAMPOSST, a new version of the MAMPOSST code of [Mamon et al. \(2013\)](#) developed to determine galaxy clusters mass profiles by analysing the internal kinematics of member galaxies in the cluster. Given an input of projected positions of member galaxies and line of sight velocities, coming either from simulated or real clusters, the code solves the Jeans equation to reconstruct the local gravitational potential and the velocity anisotropy profile, under the assumptions of spherical symmetry and dynamical relaxation. A key output is a likelihood analysis for the free model parameters in the mass profile function from dynamics. In a modified gravity scenario, the gravitational potential receives a contribution from the additional degrees of freedom, producing an effective mass profile which differs from GR. The first version of MG-MAMPOSST has been presented in Paper I for the case of linear $f(\mathcal{R})$ gravity, and has been applied to data of two galaxy clusters analysed within the CLASH/VLT collaborations ([Postman et al. 2012](#); [Rosati et al. 2014](#)). In the current version, we have extended the code’s capability by implementing two popular and viable modifications of gravity: chameleon and beyond Horndeski gravity. These models represent two distinct screening mechanisms, namely the chameleon and Vainshtein ones, respectively. They are characterised by their own phenomenological impact on the inferred mass profile from kinematical data and require a specific study of their behaviour in this context.

The MG-MAMPOSST method is complemented by CLUSTERGEN, a Python3 code capable of generating synthetic galaxy clusters in a configuration of dynamical equilibrium, which can be used to perform tests of MG-MAMPOSST and forecasting analyses neglecting all the systematic effects.

Our main goal is to showcase the code for the aforementioned class of modified gravity models, and present an analysis of statistical degeneracy between the free parameters of the model, which will be essential when testing against real data. Therefore, we will focus on a catalog of synthetic dark matter haloes produced by means of CLUSTERGEN. By assuming the availability of additional information on the galaxy cluster mass profiles, such as that provided by reliable lensing analyses, we also forecast future constraints on the modified gravity parameters, through a proper implementation of the modified gravity dynamics in the Jeans equation. In a future paper, we will present an analysis of real galaxy cluster data. We parametrise the gravitational potential assuming Navarro-Frenk-White model (NFW hereafter) of [Navarro et al. \(1997\)](#) for the matter density perturbations. The NFW profile has been widely adopted and it has been shown to provide adequate fit for simulated DM haloes and for real clusters’ data, both in GR (e.g. refs. [Biviano et al. 2013](#); [Umetsu et al. 2016](#); [Peirani et al. 2017](#)) and in modified gravity (e.g. [Lombriser et al. 2012a](#); [Wilcox et al. 2016](#)).

The paper is structured as follows. In Section 2 we present a brief summary about the two modified gravity models of this work. In Section 3 we present the MG-MAMPOSST code, its features and the new modules implemented with respect to the original version of [Mamon et al. \(2013\)](#). We further

Screening type	Models	Key eqn’s
Chameleon	$f(\mathcal{R})$, Brans-Dicke	(1)
Vainshtein	Beyond Horndeski, DHOST	(7), (11)

Table 1. The two distinct families of models considered in this work labelled according to their screening mechanism. Notice that, the linear Horndeski model described in the text is a very special case of the chameleon models where the chameleon mechanism is switched off, leading to the standard Yukawa force. For more details, we refer to the discussion of Section 2.

introduce the main properties of CLUSTERGEN, the generator of synthetic haloes accompanying MG-MAMPOSST. Sections 4 and 5 are dedicated to the applications of MG-MAMPOSST over a set of simulated dark matter haloes in the case of beyond Horndeski and chameleon gravity respectively. In Section 6 we discuss our results and main conclusions.

2 Chameleon and Vainshtein screened theories

The vast majority of scalar-tensor theories rely on a screening mechanism to recover agreement with local gravity tests at small scales. The dominant screening mechanisms are the so-called chameleon and Vainshtein mechanism (see e.g. [Koyama & Sakstein 2015](#)), and the current version of the MG-MAMPOSST code implements families of theories associated with both mechanisms.

In the presence of a screening mechanism, the fifth force that modifies the gravitational interaction w.r.t. GR is allowed to operate on sufficiently large scales, but gets suppressed locally. Both chameleon and Vainshtein mechanisms rely on the non-linear interactions of the scalar field to weaken the coupling between the scalar field and matter. However, each of them operates differently: whereas chameleon screening needs the non-linear potential interactions of the scalar, Vainshtein relies on higher-order derivative self-interactions of the scalar field. Luckily, neither one does not completely eliminate the trace of the fifth force, but leaves a characteristic imprint at local scales. Typical examples of theories exhibiting chameleon screening are conformally-coupled models such as $f(\mathcal{R})$ models or scalar-tensor models of the Brans-Dicke type. On the other hand, Vainshtein screening is a natural feature of the more general interactions in Horndeski, beyond Horndeski and DHOST scalar-tensor theories. The (derivative) interactions present in the latter theories generalise the simpler conformally-coupled interactions. In the following, in order to simplify the language, we choose to classify the models based on their screening mechanism, and we will refer to the conformally-coupled theories just as “**chameleon screening (CS) models**”, and to those exhibiting more general interactions as “**Vainshtein screening (VS) models**”. Indeed, the character of the underlying interactions is closely related to the associated type of screening operating in the theory. The “**linear Horndeski**” models which we will discuss later, correspond to a special case of conformally-coupled models where the chameleon screening is switched off, hence leading

to a standard (unsuppressed) Yukawa force mediated by the scalar. An overview of the models considered in our work can be found in Table 1.

The different phenomenology of CS and VS mechanisms is due to the structurally distinct way the resulting fifth force depends on the source's density or its gradients. In theories with chameleon screening, the fifth force is sourced by the scalar field ϕ (e.g. Khoury 2013),

$$\nabla^2 \phi = \frac{\partial V}{\partial \phi} + Q \frac{\rho}{M_{\text{P}}} e^{Q\phi/(M_{\text{P}}c_L^2)}, \quad (1)$$

where $M_{\text{P}} = (8\pi G)^{-1/2}$ is the reduced Planck mass, G is the Newton's constant and c_L is the speed of light. Q is a dimensionless coupling constant¹, ρ the density of the matter field and $V(\phi)$ is the potential of the scalar field and is a monotonic function of ϕ . A typical form of the potential assumes a power-law $V(\phi) = \Lambda^{4+n} \phi^{-n}$ where n and Λ are constants. The quantity ϕ/M_{P} has the dimension of energy per unit mass. The above equation captures a wide range of theories depending on the value of the coupling Q . In particular, $Q = 1/\sqrt{6}$ for $f(\mathcal{R})$ gravity.

Deep within the massive source, the scalar field is everywhere close to a minimum value ϕ_s and field gradients are negligible $\nabla^2 \phi \approx 0$ (see e.g. Khoury & Weltman 2004 for details). Thus, from eq. (1) we obtain the solution of the scalar field inside the source:

$$\phi_{\text{int}} \approx \left(Q \frac{\rho}{n\Lambda^{4+n}M_{\text{P}}} \right)^{-1/(n+1)}, \quad (2)$$

where we have used the power-law expression for the scalar potential and we have assumed $Q\phi/(M_{\text{P}}c_L^2) \ll 1$. In this regime, the fifth-force is screened.

Towards the outskirts of the source, the gradient of the field grows, and leads to a fifth-force per unit mass given by

$$F_\phi = -\frac{Q}{M_{\text{P}}} \frac{d\phi}{dr}, \quad (3)$$

such that the gradient of the gravitational potential is modified as

$$\frac{d\Phi}{dr} = \frac{GM(r)}{r^2} + \frac{Q}{M_{\text{P}}} \frac{d\phi}{dr}. \quad (4)$$

where $M(r)$ is the mass of the object enclosed within radius r . Note that, above and in the following, we compute the gradient of the gravitational potential assuming spherical symmetry. Far away from the massive body, the Laplacian term dominates over the field potential (i.e. $\partial V(\phi)/\partial \phi \ll \nabla^2 \phi$) and the equation of motion for the exterior chameleon field is given by:

$$\nabla^2 \phi_{\text{ext}} \approx Q \frac{\rho}{M_{\text{P}}}. \quad (5)$$

For $f(\mathcal{R})$ gravity, the additional degree of freedom is expressed in terms of the scalaron field (e.g. Barrow & Cotsakis 1988)

$$|f_{\mathcal{R}}| \equiv \left| \frac{df}{d\mathcal{R}} \right| = \exp \left[-\sqrt{\frac{2}{3}} \frac{\phi}{M_{\text{P}}c_L^2} \right] - 1. \quad (6)$$

¹ In the literature the coupling constant is often indicated by β . Throughout this paper we use Q instead to avoid confusion with the anisotropy profile parameter (see Section 3).

Equations (2) and (5) require the input of a profile for the matter density ρ in order to be solved. In this work, we will model the halo mass density assuming a NFW profile (Navarro et al. 1997) and, following e.g. Terukina & Yamamoto (2012), we will use an analytical approximation for the chameleon field radial profile $\phi(r)$ matching the inner and outer solutions (see Section 3). Given such an expression for $\phi(r)$, one can use Eq. (3) to derive the force acting on a test particle.

For beyond Horndeski and DHOST theories, which agree with gravitational wave observations, it has been shown that the Vainshtein screening mechanism is partly broken within massive sources. This leads to a different fifth force term, which does not depend only on the source's density, but also on its gradient (Kobayashi et al. 2015; Crisostomi & Koyama 2018; Dima & Vernizzi 2018):

$$\frac{d\Phi}{dr} = \frac{GM(r)}{r^2} + \frac{Y_1 G}{4} \frac{d^2 M}{dr^2}. \quad (7)$$

Here, Y_1 is the dimensionless coupling of the new force. The gradient of the mass profile is $dM(r)/dr = 4\pi\rho(r)r^2$, where ρ is the total mass density. In a galaxy cluster, the density $\rho(r)$ is assumed to be the total matter density. Expressing the second derivative of the mass in terms of matter density we find:

$$\frac{d\Phi}{dr} = \frac{GM(r)}{r^2} \left[1 + \frac{3}{4} Y_1 \left(\frac{\rho(r)}{\bar{\rho}(r)} \right) \left(2 + \frac{d \ln \rho}{d \ln r} \right) \right]. \quad (8)$$

where $\bar{\rho}(r)$ is the average density at radius r . Notice that, outside the mass distribution, the fifth-force effect vanishes because $\rho(r) \ll \bar{\rho}(r)$. What is more, the fifth force becomes zero at the scale radius r_s where the logarithmic slope of $\rho(r)$ equals -2 , regardless of the choice of the mass profile. For a given acceleration, a value $Y_1 > 0$ leads to a lower mass with respect to GR in the region $r < r_s$, while it increases the mass for $r > r_s$. The opposite happens for $Y_1 < 0$.

Eq. (8) can be expressed in a Poisson GR-like form by defining an effective dynamical mass such that

$$\frac{d\Phi}{dr} \equiv \frac{GM_{\text{dyn}}}{r^2} = \frac{G}{r^2} (M + M_1), \quad (9)$$

where

$$M_1 = Y_1 \pi r^3 \left(2\rho + r \frac{d\rho}{dr} \right). \quad (10)$$

Currently, the most stringent upper and lower bounds are of the order $|Y_1| < 10^{-2} - 10^{-1}$ and come from astrophysical probes (Sakstein 2013, 2015b,a; Jain et al. 2016; Babichev et al. 2016; Dima & Vernizzi 2018; Saltas et al. 2018; Sakstein 2018; Creminelli et al. 2018; Babichev & Lehébel 2018; Ishak 2019; Saltas & Lopes 2019; Crisostomi et al. 2019), while, on cosmological scales, constraints on Y_1 obtained with galaxy clusters are only of order unity (e.g. Sakstein et al. 2016). Note that the analyses on small and large scales are based on totally different physics, thus offer two independent and complementary ways to test the universality of the coupling constant in these models.

A fundamental difference between the two previous theories is that, whereas conformally-coupled theories such as $f(\mathcal{R})$ leave lensing unaffected, this is no longer true within beyond Horndeski and DHOST theories. In the latter case,

the relativistic potential Ψ is also modified explicitly as

$$\frac{d\Psi}{dr} = \frac{GM(r)}{r^2} - \frac{5Y_2G}{4r} \frac{dM}{dr}, \quad (11)$$

where Y_2 is a dimensionless coupling constant. As we did for Eq. (7), we can rewrite Eq. (11) highlighting the modified gravity contribution in the following way:

$$\frac{d\Psi}{dr} = \frac{GM(r)}{r^2} \left[1 - \frac{15}{4} Y_2 \left(\frac{\rho}{\bar{\rho}} \right) \right]. \quad (12)$$

Lensing is sourced by the combination

$$\Phi_{\text{lens}} = \frac{1}{2}(\Phi + \Psi), \quad (13)$$

and it may provide constraints on the additional coupling Y_2 present in these theories (e.g. Sakstein 2018). In particular, the lensing potential Φ_{lens} obeys a GR-like Poisson equation $\nabla^2 \Phi_{\text{lens}} = 4\pi G \rho_{\text{lens}}$, with

$$\rho_{\text{lens}} = \left(1 + \frac{3}{4} Y_1 - \frac{15}{8} Y_2 \right) \rho + \left(\frac{3}{4} Y_1 - \frac{5}{8} Y_2 \right) r \frac{d\rho}{dr} + \frac{Y_1}{8} r^2 \frac{d^2\rho}{dr^2}. \quad (14)$$

From the above equation, we can define an effective lensing mass which, assuming spherical symmetry, is given by

$$M_{\text{lens}} = \frac{r^2}{2G} \left[\frac{d\Psi}{dr} + \frac{d\Phi}{dr} \right] = M + \pi r^3 \left[\left(Y_1 - \frac{5}{2} Y_2 \right) \rho + \frac{Y_1}{2} r \frac{d\rho}{dr} \right], \quad (15)$$

Note that M_{lens} is sensitive to both Y_1 and Y_2 . This will be useful in analyses where dynamical probes are combined with lensing measurements. The effective lensing mass can be further expressed in terms of the dynamical mass as $M_{\text{lens}} = M_{\text{dyn}} + M_2$, where

$$M_2 = -\pi r^3 \left[\left(Y_1 + \frac{5}{2} Y_2 \right) \rho + \frac{Y_1}{2} r \frac{d\rho}{dr} \right]. \quad (16)$$

3 The MG-MAMPOSSt and ClusterGEN codes

Here we introduce the main features of MG-MAMPOSSt, focusing on the new modules implemented for modified gravity. We also briefly describe the CLUSTERGEN code, which is used to produce the mock clusters for the applications of MG-MAMPOSSt presented in Sections 4 and 5.

A. MG-MAMPOSSt

MG-MAMPOSSt is a new version of the MAMPOSSt code of Mamon et al. (2013) for the dynamical analysis of collisionless systems aimed at constraining modified gravity models. The method has been first applied in Paper I for the simple case of linear $f(\mathcal{R})$ gravity. The upgraded version of the code implements general non-linear chameleon screening and Vainshtein screening.

Main concept: The MAMPOSSt (Modelling Anisotropy and Mass Profile of Spherical Observed Systems) procedure, originally developed by Mamon et al. (2013), infers the mass profile and velocity anisotropy profile of galaxy clusters under

the assumption of spherical symmetry and dynamical relaxation. The code uses the projected information on the cluster member galaxies, which are considered as collisionless tracers of the gravitational potential, i.e. the projected distances, R , from the cluster center (hereafter, projected radii) at which a galaxy is seen by the observer, and the line-of-sight (l.o.s.) velocities, computed in the rest frame of the cluster. Working in this projected phase space (R, v_z) , MAMPOSSt performs a Maximum Likelihood fit by solving the stationary spherical Jeans equation,

$$\frac{d(v\sigma_r^2)}{dr} + 2\beta(r) \frac{v\sigma_r^2}{r} = -v(r) \frac{d\Phi}{dr}. \quad (17)$$

In the above equation, $v(r)$ corresponds to the number density profile of tracers, σ_r^2 is the squared velocity dispersion along the radial direction, $\beta \equiv 1 - (\sigma_\theta^2 + \sigma_\phi^2)/2\sigma_r^2$ is the velocity anisotropy profile and Φ is the total gravitational potential, which can provide a definition for the dynamical mass profile as

$$\frac{d\Phi}{dr} = \frac{GM_{\text{dyn}}(r)}{r^2}. \quad (18)$$

Anisotropy profile: The anisotropy profile $\beta(r)$ is not known in principle and poses one of the major systematics in the dynamical mass-profile reconstruction. To infer it, both parametric (e.g. Mamon et al. 2013; Brok et al. 2013; Read et al. 2021) and non-parametric methods have been developed. The first non-parametric determination of the velocity anisotropy profile was performed by Binney & Mamon (1982) and then improved by other works (e.g. Mamon et al. 2019 and references therein). In MG-MAMPOSSt, we adopt a parametric approach with six different models as in the original version of Mamon et al. (2013). However, for illustrative purposes, we will rely only on the anisotropy model of Tiret et al. (2007),

$$\beta_T(r) = \beta_\infty \frac{r}{1 + r\beta}, \quad (19)$$

where β_∞ is the velocity anisotropy for $r \rightarrow \infty$ and $r\beta$ is the characteristic radius of $\beta_T(r)$ (anisotropy radius).

Velocity and number density profiles: The expression for the radial velocity dispersion can be obtained by integrating Eq. (17) (e.g. Mamon & Lokas 2005)

$$\sigma_r^2(r) = \frac{1}{v(r)} \int_r^\infty \exp \left[2 \int_r^s \frac{\beta(t)}{t} dt \right] v(s) \frac{d\Phi}{ds} ds, \quad (20)$$

and the *local* l.o.s. velocity dispersion is (Binney & Mamon 1982)

$$\sigma_z^2(r, R) = \left[1 - \beta(r) \left(\frac{R}{r} \right)^2 \right], \quad (21)$$

In our current version of the code we assume that the three-dimensional distribution of the velocity field is Gaussian, as all previous applications of MAMPOSSt. Note that there is no *a priori* restriction on the choice of the 3D velocity profile. However, the tests performed by Mamon et al. (2013) over a set of haloes from cosmological simulation showed that the Gaussian model works sufficiently well even when the l.o.s. velocity distribution exhibits significant deviations from Gaussianity. The number density $v(r)$ can in general be measured directly from the phase space. As such, it can be excluded from the fit. We assumed that the tracer density

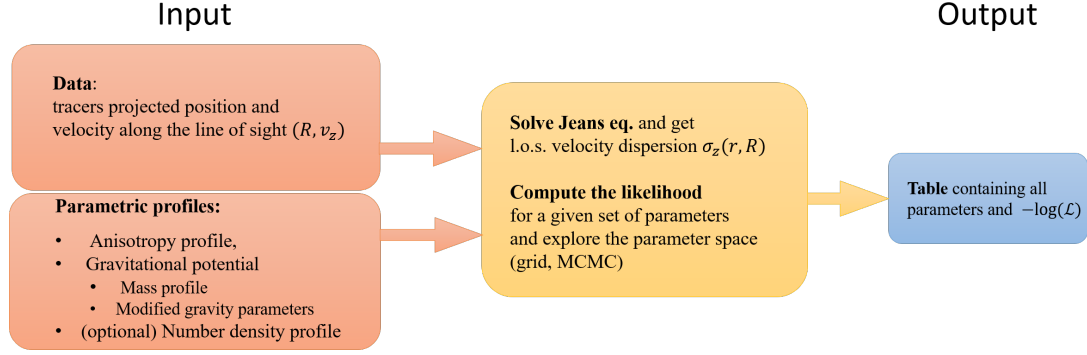


Figure 1. Diagram which illustrates the structure of the MG-MAMPOSSt code.

profile $\nu(r)$ follows an NFW model. Since the normalization of the profile is factored out in Eq. (20) the model is entirely parametrised by the scale radius r_ν of the tracer. In general, the distribution of the cluster’s members differs from the distribution of the total matter density (see e.g. Biviano & Salucci 2006; Budzynski et al. 2012; Mamon et al. 2019). Therefore, the scale radii r_ν of the tracer density and r_s of the total mass profile do not need to coincide. For additional information about the anisotropy models and mass profiles implemented in the original version, see Mamon et al. (2013).

Code output and sampling features: MG-MAMPOSSt constrains the free parameters for the mass and anisotropy profile, as well as for the gravity theory under study. The output of the code is the logarithm of the total likelihood as

$$-\ln \mathcal{L}_{\text{dyn}} = -\sum_{i=1}^N \ln q(R_i, v_{z(i)}|\theta). \quad (22)$$

In Eq. (22), N is the number of member galaxies considered in the fit, $q(R_i, v_{z(i)}|\theta)$ is the probability of observing a galaxy with projected position R_i and l.o.s. velocity $v_{z(i)}$ given the model(s) described by the set of parameters θ , where

$$q(R, v_z) = \frac{2\pi R g(R, v_z)}{N_{\text{proj}}(R_{\text{max}}) - N_{\text{proj}}(R_{\text{min}})}, \quad (23)$$

where $N_{\text{proj}}(R)$ is the predicted number of galaxies in the cylinder of projected radius R , whose axis passes through the cluster center, R_{max} and R_{min} represent the maximum and minimum projected radii considered in the fit, respectively and $g(R, v_z)$ is the surface density of observed objects with l.o.s. velocity v_z . Under the assumption of a 3D-Gaussian distribution for the velocity field, one has (Mamon et al. 2013)

$$g(R, v_z) = \sqrt{\frac{2}{\pi}} \int_R^\infty \frac{r\nu(r)}{\sigma_z(R, r)\sqrt{r^2 - R^2}} \exp\left[-\frac{v_z^2}{2\sigma_z^2(R, r)}\right] dr, \quad (24)$$

with $\sigma_z(R, r)$ given by eq. (21).

In MG-MAMPOSSt, likelihoods are computed over a multi-dimensional grid of values in the parameter space. However, for a large number of parameters ($\gtrsim 4$) the grid is computationally too expensive when the code runs in Modified Gravity mode. In order to make our analysis

more efficient, we have implemented a Monte Carlo-Markov Chain (MCMC) module, in which the chain is based on a simple Metropolis-Hastings algorithm with a fixed-step Gaussian random walk. This is particularly useful to perform forecasts over simulated catalogs with several haloes.² Fig. 1 summarizes the structure of MG-MAMPOSSt.

Gravitational potential: Compared to the original MAMPOSSt code, MG-MAMPOSSt introduces new parametrisations for the gravitational potential in Eq. (20). All the models are based on a NFW mass density profile, but the next version of the code will extend this to other mass profiles. The gravitational potentials implemented in the current version are as follows:

1. *Linear Horndeski models:* These models have been introduced in the first version of MG-MAMPOSSt and correspond to a subclass of Horndeski theories where the Newtonian potential Φ can be written in terms of three parameters, namely h_1 , Q^2 and m (see Paper I and references therein). These parameters are functions of redshift, but they can be considered constant at first approximation. In this class of models, there is no screening at all. In order to pass the local gravity constraints, either one assumes a very small coupling, or that the baryons are not sensitive to the fifth force. Here, we mention the Linearized Horndeski parameterisation for completeness. However, since the model has been already presented and tested in Paper I, we will not discuss this case any further in this paper.

2. *Vainshtein Screening:* The form of the gravitational potential is according to Eq. (7). The coupling constant Y_1 is the additional free parameter, along with the mass profile and velocity anisotropy parameters. We assume a NFW mass profile to parametrise the density perturbations:

$$\rho(r) = \frac{\rho_s}{r/r_s(1+r/r_s)^2}, \quad (25)$$

² The public version of MAMPOSSt of Mamon et al. (2013) (<https://gitlab.com/gmamon/MAMPOSSt>) is already equipped with an MCMC algorithm based on the CosmoMC package (Lewis & Bridle 2002, <https://cosmologist.info/cosmomc/>). We are planning to include CosmoMC in our MG-MAMPOSSt version for future applications.

with ρ_s the characteristic density and r_s the scale radius at which the logarithmic derivative of the density profile equals -2 . In this case, Eq. (8) can be rewritten as

$$\frac{d\Phi_{\text{MG}}}{dr} = \frac{GM_{\text{NFW}}(r)}{r^2} \left\{ 1 + \frac{Y_1}{4} \frac{r^2(r_s - r)/(r_s + r)^3}{[\ln(1 + r/r_s) - r/(r_s + r)]} \right\}, \quad (26)$$

where

$$M_{\text{NFW}}(r) = M_{200} \frac{\ln(1 + r/r_s) - (r/r_s)/(1 + r/r_s)}{\ln(1 + c) - c/(1 + c)} \quad (27)$$

is the standard NFW mass profile in GR, and $c = r_{200}/r_s$ is the concentration. In the above equation $M_{200} = 4\pi r_s^3 \rho_s [\ln(1 + c) - c/(1 + c)]$ is the total mass of a sphere of radius r_{200} enclosing an average matter density 200 times the critical density of the Universe at that redshift $\rho_c(z) = 3H^2(z)/(8\pi G)$.

According to Eq. (9), the contribution induced by the modification of gravity is given by

$$M_1(r) = M_{200} \frac{Y_1 r^2 (r_s - r)}{4 (r_s + r)^3} \times [\ln(1 + c) - c/(1 + c)]^{-1}. \quad (28)$$

In the top left plot of Fig. 2 we show the ratios of modified to Newtonian (GR) gravitational potentials. The profiles are computed adopting an NFW model with $r_{200} = 2.0 \text{ Mpc}$, $r_s = 0.3 \text{ Mpc}$ for two different fifth-force coupling values, $Y_1 = 0.1$ (blue line) and $Y_1 = -0.1$ (red line). These values are consistent with current bounds derived from astrophysical probes (e.g. Sakstein 2018; Creminelli et al. 2018; Saltas et al. 2018). In the case of $Y_1 > 0$ the potential gradient (i.e. the effective dynamical mass) is enhanced with respect to GR for radii smaller than r_s and damped at large r . Exactly the opposite happens for $Y_1 < 0$. In the top right panel of 2 we plot the corresponding ratios of l.o.s. velocity dispersions. The integration has been performed by using eq. (A15) of Mamon & Lokas (2005) where for the velocity anisotropy profile we have used the Tiert model with $\beta_\infty = 0.5$ and $r_\beta = r_s^3$. For realistic values of the coupling parameter, the effect on cluster's internal kinematics is very small (order of $\sim 10^{-2}$). We thus expect that the constraints derived with the MG-MAMPOST procedure alone cannot reach the level of accuracy as those from astrophysical analyses.

3. General Chameleon Screening: For this class of models the gravitational potential is given by Eq. (4). As mentioned in Section 2, for the chameleon field ϕ we use an analytic approximation that matches the two limiting solutions inside ($\nabla^2 \phi \approx 0$) and outside the object ($\partial V/\partial \phi$ is subdominant). In the case of an NFW mass density profile, the field profile reads

$$\phi(x) = \begin{cases} \phi_s [x(1+x)^2]^{1/(n+1)} \equiv \phi_{\text{int}}(x) & r < S \\ -\frac{Q\rho_s r_s^2}{M_P} \frac{\ln(1+x)}{x} - \frac{C}{x} + \phi_\infty \equiv \phi_{\text{ext}}(x) & r > S. \end{cases} \quad (29)$$

In the above equation we have defined $x = r/r_s$, ϕ_∞ is the background value of the field, C is an integration constant

and

$$\phi_s \equiv \left(\frac{n\Lambda^{n+4} M_P}{Q\rho_s} \right)^{1/(n+1)}.$$

The *screening radius* S represents the transition scale between the two regimes. C and S can be determined requiring that ϕ_{int} and ϕ_{ext} and their derivatives match at S . In the halo's inner core the field is strongly suppressed with respect to its ambient value $\phi_s \ll \phi_\infty$, and we can approximate the interior solution to be negligible $\phi_{\text{int}} \simeq 0$. In this case, for C and S ,

$$S = \frac{Q\rho_s r_s^3}{M_P \phi_\infty} - r_s, \quad (30)$$

$$C = -\frac{Q\rho_s r_s^2}{M_P} \ln(1 + S/r_s) + \phi_\infty S/r_s. \quad (31)$$

Chameleon $f(\mathcal{R})$ gravity is included as the sub-class obtained for $Q = 1/\sqrt{6}$.

While for linear Horndeski and VS models the modified gravity parameters are independent of the size of the halo, in CS the suppression of the fifth force is related to the matter density. In particular, as we will show in Section 5, clusters with smaller mass and larger r_s have a screening mechanism less efficient with respect to more massive haloes.

In the bottom plots of Fig. 2, we show the relative ratio of mass profiles in CS with respect to GR obtained for different values of Q and ϕ_∞ . For a large background field, the cluster is not screened and the effective mass profile is enhanced of a factor $2Q^2$ compared to the standard NFW model. Decreasing ϕ_∞ , the screening mechanism becomes active and $M_{\text{dyn}} \equiv M_{\text{NFW}}$ for $r \leq S$. Grey curves show the effective mass profiles for a chameleon field $\phi_\infty = 10^{-4}$ and a coupling constant $Q = 1$ – since the screening effect is connected to the coupling with matter, part of the halo is screened, while the fifth force increases in the non-screened region. The bottom left plot of Fig. 2 refers to more massive halo with higher concentration with respect to the bottom right plot (see details in the caption of the Figure). As expected, in this second case the screening suppression is reduced and the effect of the fifth force is enhanced also for small field values.

B. ClusterGEN

The CLUSTERGEN code, first presented in Pizzuti et al. (2019) is a generator for isolated, self-gravitating systems in dynamical equilibrium, populated by collisionless point-like tracers according to a spherical model. The code produces mock-data catalogs which serve as input for MG-MAMPOST. The main purpose is to test the constraining power of the MG-MAMPOST method for different modified gravity scenarios in ideal conditions where all the systematics are under control. The synthetic clusters can be built with different characteristic masses and scales, while the internal kinematics is assumed to be governed by the Jeans equation (17) with a 3D Gaussian local velocity distribution function (VDFs). Now dynamical systems may have non-Gaussian local VDFs. The correct way to build a simulated spherical system in dynamical equilibrium is to use six-dimensional distribution functions, expressed in terms of the binding energy and angular momentum (Kazantzidis et al. 2004), or in terms of action-angle variables (Vasiliev 2019). However, the

3 As for the number density profile, we still assume a NFW with $r_v \equiv r_s$

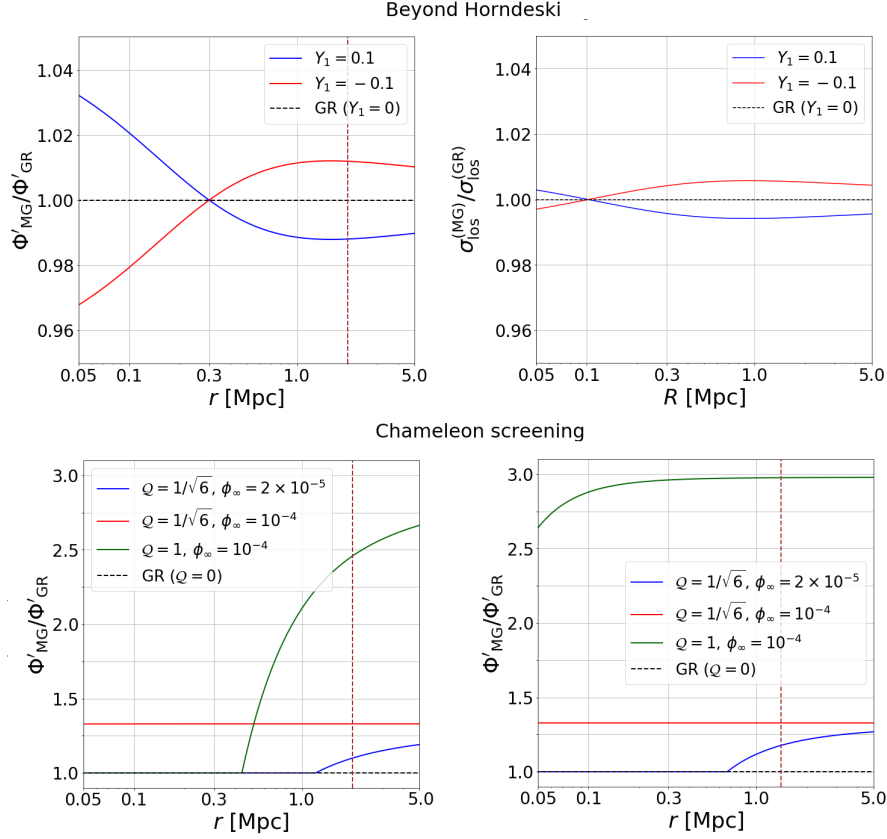


Figure 2. *Top left:* Ratios of the potential gradients as a function of the distance from the cluster center, for a NFW halo with $r_{200} = 2.0$ Mpc, $r_s = 0.3$ Mpc. The profiles $\Phi'_{\text{MG}}(r)$ are obtained in a VS model with $Y_1 = 0.1$ (red curves) and $Y_1 = -0.1$ (blue curves), values compatible with current astrophysical constraints, while Φ'_{GR} represents the derivative of the Newtonian potential. *Top right:* Ratios of the corresponding velocity dispersion profiles $\sigma_{\text{los}}(R)$, integrated along the line of sight, at a projected position R . *Bottom:* Ratios of the potential gradients in CS gravity with $Q = 1/\sqrt{6}$, $\phi_\infty = 10^{-4}$ (red curves), $Q = 1/\sqrt{6}$, 2×10^{-5} (blue curves) and $Q = 1$, $\phi_\infty = 10^{-4}$ (green curves). The left plot shows profiles derived from a NFW halo with $r_{200} = 2.0$ Mpc, $r_s = 0.3$ Mpc while the right plot is for haloes with $r_{200} = 1.4$ Mpc, $r_s = 0.33$ Mpc. The vertical brown dashed lines in the left plots and in the bottom right plot represent the radius r_{200} .

MAMPOSSt procedure has been shown to work quite well in recovering the mass density and anisotropy profile of galaxy clusters (e.g. Mamon et al. 2013; Old et al. 2015) and dwarf spheroidal galaxies (Read et al. 2021) assuming a Gaussian local VDF. In this paper, we aim to test MG-MAMPOSSt in an ideal scenario where the mass profile reconstruction is unbiased with respect to the set of synthetic haloes. As such, our mock catalog, generated by assuming a 3D Gaussian local VDF, provides useful hints to study the degeneracy between the free parameters of the model in a modified gravity framework.

For a given radial number density profile, CLUSTERGEN distributes the particles in spherical shells from the cluster center and assigns to each tracer a velocity whose components, in spherical coordinates, have a squared dispersion $\sigma_{\mathbf{r}}^2(r) = \{\sigma_r^2(r), \sigma_\theta^2(r), \sigma_\phi^2(r)\}$, where $\sigma_r^2(r)$ is given by the integral solution Eq. (20), while $\sigma_\theta^2(r) = \sigma_\phi^2(r) = [1 - \beta(r)]\sigma_r^2$.

The current version of CLUSTERGEN works with four different anisotropy models, namely constant anisotropy $\beta(r) = \beta_C$ (which reduces to the isotropic case when $\beta_C = 0$), the Mamon & Lokas profile, the Tiret profile and the modified Tiret profile (see e.g. Biviano et al. 2013), which allows for negative anisotropy in the halo center. As for the gravitational poten-

tial, the radial velocity dispersion of Eq. (20) can be obtained both assuming GR as well as with one of the modified gravity models implemented in the MG-MAMPOSSt code. In this work, we only consider GR-based mock catalogues, leaving the analysis of non-GR mock haloes for future applications.

The projected phase space (R, v_z) used as input data for MG-MAMPOSSt is generated from the six-dimensional phase space using $R = (x^2 + y^2)^{1/2}$. In Fig. 3, we plot two phase spaces obtained for one cluster in our catalog (see next Section for halo's parameters details) considering $N = 600$ particles (left) and $N = 100$ particles (right) within the virial cylinder ($R < r_{200}$).

4 Application I: Vainshtein screening

In this Section, we show the application of MG-MAMPOSSt for the choice of VS, to spherically-symmetric and virialised synthetic clusters generated with the CLUSTERGEN code as outlined in Section 3. We investigate the possible constraints on the additional degree of freedom Y_1 from internal kinematics analysis alone and simulating the availability of additional

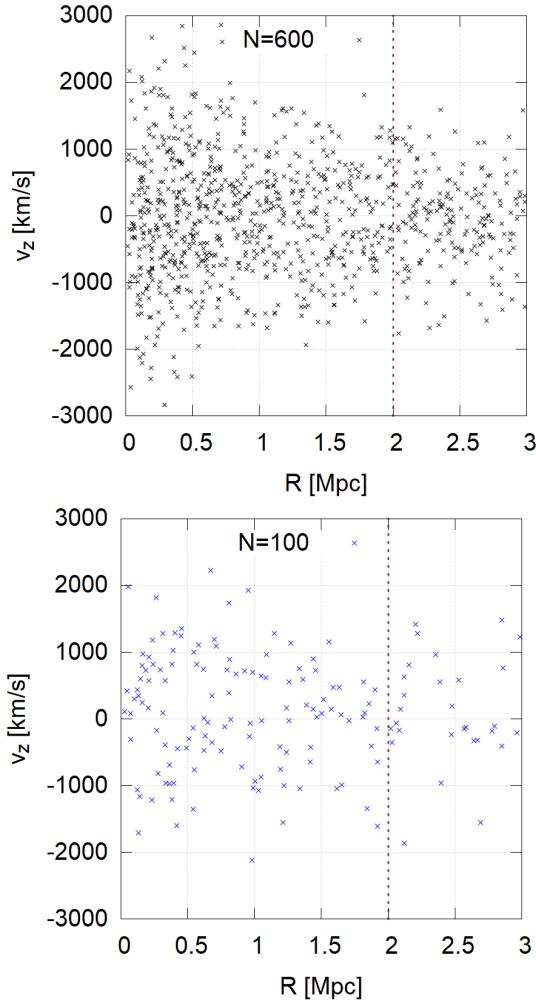


Figure 3. Projected phase spaces for a standard NFW halo with $r_{200} = 2.0$ Mpc, $r_s = 0.3$ Mpc, assuming a Tired model for the velocity anisotropy profile with $r_\beta = r_s$ and $\beta_\infty = 0.5$. Up: 600 tracers considered within r_{200} (vertical brown dashed line). Bottom: 100 tracers within r_{200} .

information such as the probability distribution provided by a strong+weak lensing probe.

4.1 Setup

For VS models, modifications of gravity are not related to the size of the halo considered. Thus, all synthetic phase spaces are generated as different realization of the same massive NFW halo with $r_{200} = 2.0$ Mpc, $r_s = 0.3$ Mpc, and with a Tired anisotropy profile $\beta(r) = \beta_\infty r / (r + r_\beta)$ with $r_\beta = r_s$ and $\beta_\infty = 0.5$ (i.e. Mamon & Lokas 2005). In view of the proof-of-concept aim of the paper, this choice has been made to facilitate the combined analysis of several clusters. Furthermore, in order to avoid spurious signatures of modified gravity due to statistical fluctuations in the cluster generation process, each phase space is derived requiring that the logarithm of the likelihood computed at the best fits of the standard MAMPOSS_T analysis in GR differs from the one computed at the cluster true values by less than 1%. This

way, the obtained constraints reflect the true statistical degeneracy between the model parameters.

Note that real galaxy clusters at $z < 1$ generally exhibit lower values of r_{200} and smaller concentration parameters (see e.g. Biviano et al. 2017). For example, a typical galaxy cluster of $M_{200} \sim 10^{14.5} M_\odot$ at $z = 0$ (with $h = 0.7$) has $r_{200} = 1.4$ Mpc and $r_s = 0.33$ Mpc (i.e. $c \sim 4.3$ according to e.g. Dutton & Macciò 2014). However, we have calibrated our simulations to reflect the best fit values obtained by the MAMPOSS_T analysis of the massive cluster MACS J1206.2-0847 (MACS 1206 hereafter) (Biviano et al. 2013) within the CLASH and CLASH-VLT collaborations. This has been done in view of the application of MG-MAMPOSS_T over the MACS 1206 data-set in order to obtain realistic constraints on the MG models presented here. In the case of VS models, we will see that the values of r_s and r_{200} are not relevant for the analysis since the fifth force exhibits the same structure at all scales. As we have already mentioned in Section 3 this is not true for the CS mechanism. We will discuss in Section 5 how our constraints change in this specific class of models when varying the values of the NFW parameters.

As a default choice, each synthetic cluster is constructed with 600 particles (tracers) in the radial range $[0.05 \text{ Mpc}, r_{200}]$. This choice is a reasonable, although optimistic, expectation for the number of member galaxies' spectroscopic redshifts available for few dozen clusters from ongoing and next generation surveys. It is, however, an important systematic factor in realistic observations – indeed, Jeans analysis of galaxy clusters' internal kinematics is limited by several effects, such as substructures, modeling of velocity anisotropy profiles, departures from spherical symmetry and dynamical relaxation (see e.g. Pizzuti et al. 2020 and references therein). This may produce a bias in the mass profile reconstruction even for a quite large (~ 1000) number of tracers, especially when searching for tiny deviations from standard gravity. Moreover, the new degrees of freedom could be strongly degenerate with the mass profile parameters and no constraints can be derived at all from internal kinematics (see again Pizzuti et al. 2020 for the case of linear $f(\mathcal{R})$ gravity).

We will therefore discuss how our results are affected when lowering the number of tracers considered in the synthetic phase spaces as well as when considering stacked clusters. As concerns the projected radial range, we note that for real data the dynamics of member galaxies in clusters is dominated by the Brightest Central Galaxy (BCG) in the innermost region, which is thus excluded from the analysis. Similarly, even for relaxed clusters, departures from dynamical equilibrium can become important above r_{200} . The analysis of Falco et al. (2013) showed that the Jeans equation can be still used to correctly infer the radial velocity dispersion up to $\approx 1.4 r_{200}$. However, since it is not clear what is the maximum projected radius R below which Jeans analysis is valid, we make a conservative assumption of $R_{\text{max}} = r_{200}$. For further discussions see e.g. Biviano et al. (2013); Pizzuti et al. (2019).

4.2 Kinematical analysis

We considered a catalog of 20 synthetic haloes generated in Newtonian gravity (GR). This is a fair expectation of the number of relaxed galaxy clusters for which very high quality imaging and spectroscopic data could be available from present and future surveys.

4.2.1 Single cluster

Given the tracers' phase space (R, v_z) , we first apply MG-MAMPOSSt to fit the parameters of the mass profile (r_{200}, r_s) , the anisotropy parameter (β_∞) and the modified gravity parameter Y_1 .

For the velocity anisotropy, from now on we use

$$\mathcal{A}_\infty \equiv (1 - \beta_\infty)^{-1/2} = \left(\frac{\sigma_r}{\sigma_\theta} \right)_{r \rightarrow \infty}, \quad (32)$$

as in e.g. Mamon et al. (2010), which is equal to unity for isotropic distributions $(\beta_\infty = 0)$ and to 1.41 for $\beta_\infty = 0.5$. As explained in Section 3, the fitting procedure can be performed by computing the likelihood over a multi-dimensional grid or by means of an MCMC algorithm. In this work, in order to explore more efficiently our range of parameters, we carry out the MCMC sampling over 3×10^5 points in the space $(\log(r_{200}), \log(r_s), \log(\mathcal{A}_\infty), Y_1)$. Note that we have considered the logarithm of the parameters, except for Y_1 which can be negative, in order to give an equal weight to all values. We assume flat priors in the allowed ranges of values for each parameter, listed in Table 2. The lower bounds of $Y_1 > -2/3 \simeq -0.67$ follows from the stability condition discussed in Babichev et al. (2016)

The results for the 2-dimensional marginalised isoprobability contours $2\Delta(\ln \mathcal{L})$, where $\mathcal{L} \equiv \mathcal{L}^{\text{dyn}}$ is the MG-MAMPOSSt likelihood, and the one-dimensional distributions for each parameter are shown in Fig. 4 and Fig. 5 respectively, for a single cluster.

A first important lesson is that the coupling constant Y_1 is strongly degenerate with the mass profile parameters – increasing the NFW parameters r_s and r_{200} corresponds to an increase of Y_1 respectively. This is expected, since increasing Y_1 leads to a lower gravitational potential gradient (compared to GR) for $r > r_s$, which can be compensated by assuming either a larger r_{200} or a larger r_s . As a consequence, the effect of a standard Newtonian gravitational potential in a galaxy cluster phase space can be mimicked to a certain extent by introducing an additional degree of freedom Y_1 and suitably adjusting the values of the other parameters. This aspect needs to be accounted for in the analysis of real observations when placing constraints on the modified gravity coupling.

Fig. 5 shows the marginalised, 1-dimensional likelihoods for one halo in the sample. Note that all the distributions of (Y_1, r_s, r_{200}) are shifted towards larger positive values with respect to the expectation, particularly for Y_1 . This is a statistical artifact and not a physical effect – indeed, all the four-dimensional likelihoods exhibit a maximum in the neighborhood of the halo's parameters true values (i.e. $Y_1 = 0$, $r_{200} = 2.0 \text{ Mpc}$, $r_s = 0.3 \text{ Mpc}$, $\mathcal{A}_\infty = 1.41$) by construction. However, they also have a second local maximum at $Y_1 > 1$, due to the strong degeneracy with the mass profile parameters, which shifts the 1-dimensional distribution when marginalizing. We can always set an upper limit $Y_1 < 6.92$ at $2\Delta(\ln \mathcal{L}) = 4.0$ from the marginalised distribution (corresponding to 95% C.L.). The value has been chosen as the largest constraint obtained among the 20 marginalised distributions $P(Y_1)$ of each of the synthetic phase spaces in the sample. In the bottom right plot of Fig. 5 we have also shown the marginalized distribution obtained from the MG-MAMPOSSt analysis of a halo with $r_{200} = 1.4 \text{ Mpc}$ and

$r_s = 0.33 \text{ Mpc}$ (i.e. smaller concentration and smaller mass with respect to the reference case). As expected, the two distributions are basically equivalent, modulo statistical fluctuations. This confirms that this modified gravity model is not affected by the size (or mass) of the cluster.

4.2.2 Joint clusters

So far we focused on a single cluster. Still working with the synthetic clusters constructed assuming GR, we combine the individual likelihoods of each phase space to study the joint distribution as a function of the number of haloes. We write,

$$-\ln \mathcal{L}_{\text{tot}} = \sum_i^{N_h} (-\ln \mathcal{L}_i^{\text{dyn}}), \quad (33)$$

where N_h is the number of phase spaces in the sum. Remember that we are considering realizations of haloes characterized by the same NFW parameters (i.e. the values of r_{200} , r_s and \mathcal{A}_∞ are the same for each realization), but with distinct projected phase spaces. Thus, a stacked analysis can be done by Monte-Carlo sampling over the combination of single likelihoods of different (synthetic) clusters as in Eq. (33). In Fig. 6 we plot five marginalised distributions $P(Y_1)$, corresponding to different number of haloes N_h taken into account in Eq. (33). The curves exhibit an apparent tension with $Y_1 = 0$ for $N_h > 1$. When increasing the number of haloes, the distributions develop a second maximum near the GR expectation value which, however, remains subdominant with respect to the first peak. As one may naively expect, this confirms that the statistical degeneracy, responsible of the spurious maximum in the marginalised likelihood, cannot be removed just by increasing the number of haloes in the fit. The constraints obtained at 95% C.L. are listed in the second column of Table 3. For $N_h \sim 20$ we may extract, at 95% C.L., an upper limit $Y_1 \lesssim 3.9$ and a lower limit $Y_1 \gtrsim -0.44$, marginally close to the theoretical bound, $Y_1 > -2/3$ (e.g. Saltas et al. 2018; Sakstein 2018; Creminelli et al. 2018).

The results of our analysis indicate that, in the case of VS models, the constraints obtainable with the MG-MAMPOSSt fit alone are limited by the statistical degeneracy between model parameters. Other probes, such as X-ray and lensing measurements, are required in order to remove the unphysical region of the parameter space associated to large values of r_s , r_{200} , Y_1 . Similar conclusions have been reached by Paper I for the application of MG-MAMPOSSt to linear $f(\mathcal{R})$ gravity. Therefore, although kinematics alone are not able to provide sufficiently constraining bounds on Y_1 , one may expect to obtain valuable results from the combination of several data-sets obtained with different methods. In order to further investigate this point, in the following we simulate the availability of additional lensing information to understand at what level of precision the models can be constrained with our method.

4.3 Joint Lensing and internal kinematics analysis

Present and upcoming high precision strong+weak lensing measurements can recover the mass profile parameters r_{200} and r_s with uncertainties down to $\sim 7 - 10\%$ and $\sim 30\%$ respectively (e.g. Umetsu et al. 2016). In order to forecast the

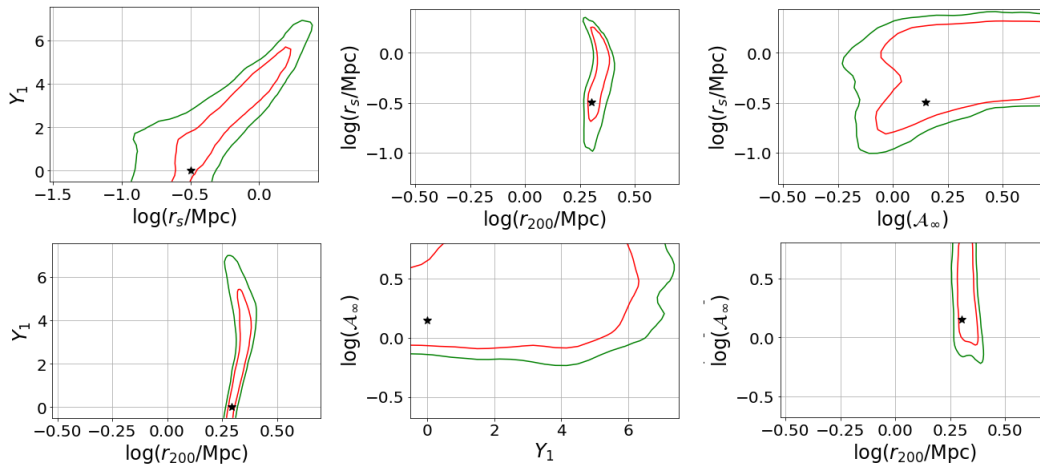


Figure 4. Iso-chi square contours of the marginalised 2-dimensional distributions for the free parameters in the MG-MAMPOSST fit, i.e. the NFW profile and modified gravity parameter Y_1 . The results are shown for one halo in the analysis, but they are representative of the behaviour of all the cluster sample. Green curves: $2\Delta(\ln \mathcal{L}) = 6.1$ contours. Red curves: $2\Delta(\ln \mathcal{L}) = 2.3$. The black stars indicate the true values of the halo's parameters.

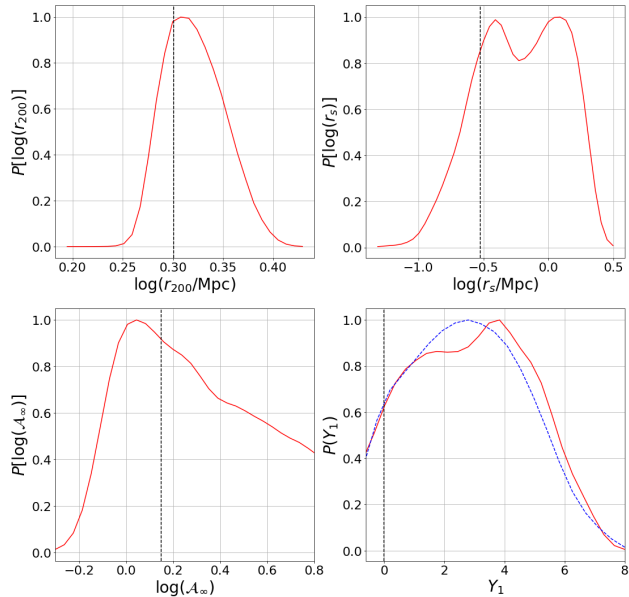


Figure 5. Marginalised one-dimensional distributions of the four free parameters obtained by the MG-MAMPOSST analysis for the same halo of Fig. 4. The vertical dashed lines represent the true value of the parameters while the blue dashed curve in the bottom right plot shows the marginalized distribution of Y_1 obtained when considering a halo with $r_{200} = 1.4$ Mpc and $r_s = 0.33$ Mpc.

constraints obtainable by our method with an additional lensing probe, we need to correctly simulate a full convergence and shear profile for our mock haloes as well as to employ a strong lensing modeling for the inner core of the cluster. Instead of implementing a full ray-tracing simulation, here we focus only on weak lensing analyses by building a mock (reduced) tangential shear profile keeping our ideal assumption of perfect control of systematic effects.

As mentioned before, we aim at applying the work presented in this paper in order to obtain constraints from a joint

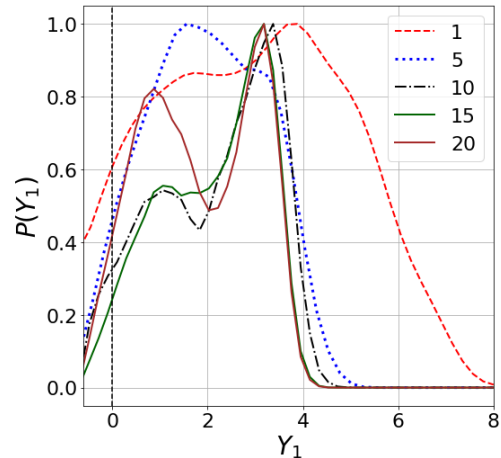


Figure 6. Marginalised distributions $P(Y_1)$ obtained by combining likelihoods of single haloes according to Eq. (33). Different curves correspond to different number of phase spaces considered in the combination. The effect of strong degeneracy between Y_1 and the NFW parameters r_s , r_{200} , is particularly evident for $N_{\text{haloes}} \geq 10$, giving rise to a spurious peak at $Y_1 > 0$.

lensing and kinematic analysis of the relaxed massive cluster MACS 1206, for which accurate strong+weak lensing profiles has been derived in GR (Umetsu et al. 2012, 2016; Caminha et al. 2017). As such, we calibrate our lensing model over an NFW halo characterised by $r_{200} = 2.0$ Mpc and $r_s = 0.3$ Mpc, located at the same redshift of MACS 1206, $z_c = 0.44$.

In the weak-lensing approximation, the distortion of the background sources is relatively small (see e.g. Kaiser et al. 1995) and the reduced tangential shear profile can be defined as:

$$g_t(R) = \frac{\gamma_t(R)}{1 - \kappa(R)}, \quad (34)$$

where κ and γ_t represent the convergence and tangential shear profiles as a function of the projected radius R . These quantities can be expressed in terms of the lens' surface mass

Parameter	Min value allowed	Max value allowed
$\log(r_{200})$	$\log(0.15 r_{200}^{\text{true}})$	$\log(2.5 r_{200}^{\text{true}})$
$\log(r_s)$	$\log(0.10 r_s^{\text{true}})$	$\log(8.0 r_s^{\text{true}})$
$\log(\mathcal{A}_\infty)$	$\log(0.15 \mathcal{A}_\infty^{\text{true}})$	$\log(5.0 \mathcal{A}_\infty^{\text{true}})$
Y_1	-0.67	8.0
Y_2	-8.0	8.0
Q_2	0	1
ϕ_2	0	1

Table 2. Allowed parameter range in the MG-MAMPOSSt fit used for all the analyses presented in this paper. The quantities r_{200}^{true} , r_s^{true} and $\mathcal{A}_\infty^{\text{true}}$ indicate the true values of the cluster's parameters. Q_2 and ϕ_2 are defined according to Eq. (46). In the case of VS, all the combinations of Y_1 and Y_2 within the ranges giving rise to a negative effective mass have been excluded from the analyses.

density

$$\kappa(R) = \frac{4\pi G}{c^2} \frac{D_1 D_{1s}}{D_s} \Sigma(R),$$

$$\gamma_t(R) = \frac{4\pi G}{c^2} \frac{D_1 D_{1s}}{D_s} [\bar{\Sigma}(R) - \Sigma(R)], \quad (35)$$

where $D_s(z_s)$, $D_l(z_c)$ are the angular diameter distances of a source located at redshift z_s and of the lens at the cluster redshift z_c , respectively. $D_{1s}(z_c, z_s)$ is the angular diameter distance between the source and the lens. Finally, $\bar{\Sigma}(R) = M_{\text{proj}}(R)/(\pi R^2)$ is the average surface mass density profile. The surface mass density is obtained with the projection equation:

$$\Sigma(R) = 2 \int_R^\infty \rho(r) \frac{r}{\sqrt{r^2 - R^2}} dr, \quad (36)$$

while the projected mass, $M_{\text{proj}}(R) = \int_0^R 2\pi S \Sigma(S) dS$ involves a double integral, which can be expressed with single integrals as

$$M_{\text{proj}}(R) = 4\pi \left[\int_0^R \rho(r) r^2 dr + \int_R^\infty \rho(r) (r^2 - r\sqrt{r^2 - R^2}) dr \right], \quad (37)$$

(Appendix A of Mamon et al. 2010). Analytical expressions for $\Sigma(R)$ and $M_{\text{proj}}(R)$ for the NFW model were first derived by Bartelmann (1996).

In order to build our mock profile, we should assume a distribution of the background sources to average the lensing convergence and tangential shear over all source redshifts. Following e.g. Chen et al. (2020) and references therein, we consider a density of sources described by

$$n(z_s) = C z_s^2 \exp\left(-\frac{z_s}{z_0}\right), \quad z_0 = \frac{1}{3} \left(\frac{n_g}{30}\right)^{1/3}. \quad (38)$$

In the above equation, C is a normalization factor and n_g is the average number of source galaxies per arcmin² observable from current and future surveys. Here we assume $n_g = 30 \text{ arcmin}^{-2}$, as expected for the Wide Survey of the Euclid mission (Laureijs et al. 2011). Furthermore, we found that varying n_g in a reasonable range – from 20 arcmin^{-2} to 40 arcmin^{-2} – produces negligible effects on our results.

For $n_g = 30$, the density distribution peaks at $z_s \sim 0.6$ and sharply decreases at higher redshift becoming negligible for $z \gtrsim 3$. The reduced tangential shear profile, averaged over all redshifts, is then given by

$$\langle g_t \rangle \simeq \frac{\langle \gamma_t \rangle}{1 - f_1 \langle \kappa \rangle}, \quad (39)$$

where the average $\langle X \rangle$ is obtained by integrating X weighted with $n(z_s)$ from z_c to the maximum redshift of the sources z_m . In the following, we set $z_m = 10$. The factor f_1 , of order unity, is given by the ratio $\langle W^2 \rangle / \langle W \rangle^2$, with $W = D_{1s}/D_s$.

We consider $N_b = 10$ log-spaced radial bins from the cluster center over the angular range $[0.6', 16']$. For the lower bound, we choose a value which is larger than the Einstein radius of the cluster ($\sim 28''$ for MACS 1206, see e.g. Umetsu et al. 2012; Zitrin et al. 2015) to ensure the validity of weak lensing approximation. The upper limit is set following the weak lensing analysis of 16 X-ray selected clusters by Umetsu et al. (2014). To each radial bin we assign an associated error $\sigma_{l,i}$ given by the quadratic sum of two contributions

$$\sigma_{l,i}^2 = \sigma_{e,i}^2 + \sigma_{\text{ISS}}^2, \quad (40)$$

where $\sigma_{e,i}^2 = \sigma_g^2 / [\pi(\alpha_{\text{up}}^2 - \alpha_{\text{low}}^2) n_g]$ is the noise due to the intrinsic ellipticity σ_g^2 of the sources lying within an annulus between the angles α_{low} and α_{up} , and σ_{ISS}^2 expresses the effect of the uncorrelated projected large scale structure (Hoekstra 2003). The full covariance matrix due to the cosmic-noise can be estimated numerically as shown by e.g. Umetsu et al. (2011) and the computation requires the knowledge of the non-linear matter power spectrum. The overall result is of the order of a few thousandths and the contribution of σ_{ISS}^2 becomes relevant only at large cluster radii (see Figure 14 of Umetsu 2020). Working in a simplified picture, we assume a constant value $\sigma_{\text{ISS}} = 0.005$ for all bins. As for σ_g , typical values of adopted in the literature vary between ~ 0.25 and ~ 0.4 (see e.g. Köhlinger et al. 2015; Chen et al. 2020). In our simulation we assume $\sigma_g = 0.3$.

The binned mock tangential shear profile for our reference NFW halo is shown in Figure 7 as a function of the projected radius $R = \alpha D_l(z_c)$.

In Section 2 we have mentioned that the lensing Poisson equation relates the effective mass density profile to the sum of the gravitational potentials. In VS models, the effective density ρ_{lens} is given by Eq. (14). Assuming a NFW model, this becomes:

$$\rho_{\text{lens}}(r) = \rho_{\text{NFW}}(r) \left[1 + \frac{Y_1 - 5Y_2 - (2Y_1 + 5Y_2) r/r_s}{4(1 + r/r_s)^2} \right], \quad (41)$$

which can be further integrated by means of Eqs. (36), (37) in order to obtain the effective tangential shear profile $g_{t,\text{vs}}(R_i | \theta_1)$ as a function of the parameter vector $\theta_1 = (r_{200}, r_s, Y_1, Y_2)$. For each choice of the free parameters, the lensing (log) likelihood is then computed as:

$$\ln \mathcal{L}_{\text{lens}}(\theta_1) = -\frac{1}{2} \sum_{i=1}^{N_b} \frac{[\langle g_t(R_i) \rangle - \langle g_{t,\text{vs}}(R_i | \theta_1) \rangle]^2}{\sigma_{l,i}^2}, \quad (42)$$

where $N_b = 10$ is the number of bins.

As done above, we perform a MCMC sampling in the space $(\log(r_{200}), \log(r_s), \log(\mathcal{A}_\infty), Y_1, Y_2)$, assuming a flat prior for each parameter within the allowed ranges, which are listed in

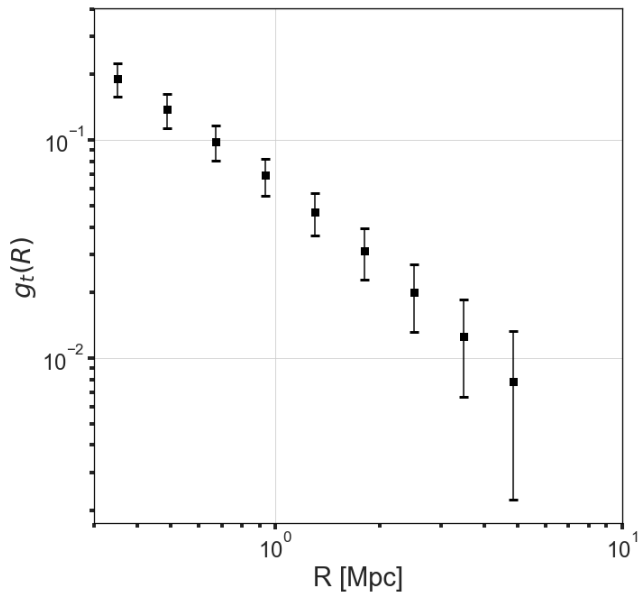


Figure 7. Mock tangential shear profile built for the reference NFW halo in our analysis, $r_s = 0.3$ Mpc, $r_{200} = 2.0$ Mpc. The error bars indicate the values of $\sigma_{1,i}$. The relative increase of the error bars at larger radii is due to the dominance of uncertainties associated to large-scale structures, as explained in the text.

Table 2. When Y_1 and Y_2 are considered, we excluded all the combinations for which the resulting mass profiles become negative. Moreover, Y_1 is assumed to be strictly larger than $-2/3$ to fulfill the stability conditions highlighted earlier. The sampling has been performed by using the joint distribution

$$\ln \mathcal{L}_{\text{joint}} = \ln \mathcal{L}_{\text{tot}}(r_s, r_{200}, \mathcal{A}_\infty, Y_1) + N_h \ln \mathcal{L}_{\text{lens}}(\theta_1),$$

where N_h indicates the number of clusters considered in the stacking analysis and $\mathcal{L}_{\text{tot}}(r_s, r_{200}, \mathcal{A}_\infty, Y_1)$ is the N_h clusters-combined MG-MAMPOST fit likelihood, Eq. (33).

The constraints at 95% C.L. on the VS parameters Y_1 and Y_2 are listed in Table 3 for different number of clusters considered in the combined analysis. In Fig. 8 we show the marginalized posterior distributions of Y_1 and Y_2 for a single halo in the sample when ~ 600 (red solid lines) and ~ 100 (blue dashed lines) tracers are considered in the MG-MAMPOST fit, compared with the posteriors from lensing only (green dash-dotted curves). Adding the internal kinematics information to the lensing posterior dramatically improves the constraint on Y_2 and strongly improves that on Y_1 . For the joint kinematic+lensing analysis of the reference case ($N = 600$), we obtain at 95% C.L.:

$$Y_1 \lesssim 2.75, \quad Y_2 = -0.08^{+0.32}_{-0.28}. \quad (43)$$

Note that for Y_1 we consider only the upper limit, as the lower bound is still given by the value settled by the stability conditions $Y > -2/3$.

As expected, our results are consistent with the GR predictions and of the same order of current cosmological bounds on those parameters derived with similar methods. In particular, Sakstein et al. (2016) obtained constraints of order unity on Y_1 and Y_2 by combining the stacked X-ray surface brightness profiles from the XMM Cluster Survey and weak lensing pro-

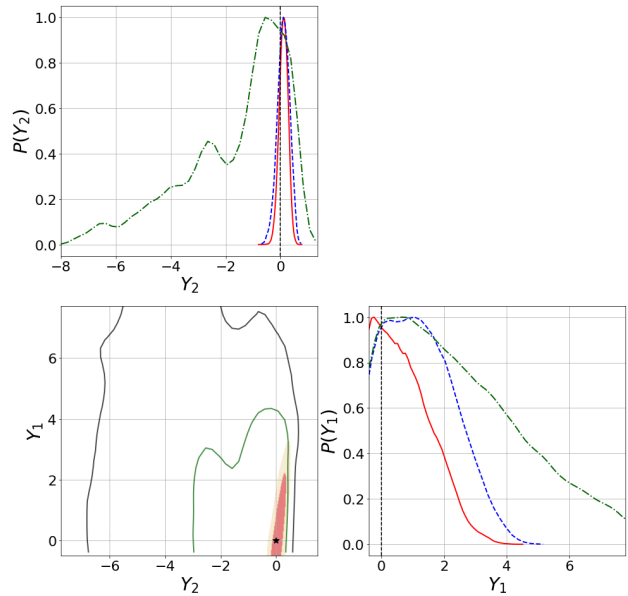


Figure 8. Bottom-left plot: two-dimensional distribution in the space (Y_1, Y_2) obtained from the lensing+kinematics likelihood of one cluster with $N = 600$ tracers in the MG-MAMPOST fit. The dark red and light red shaded areas represent the 1σ and 2σ contours, respectively, while the green and black contours refer to the same for lensing analysis only. Upper and bottom-right plots: marginal distributions of Y_1 and Y_2 for the joint lensing+kinematics analysis of the same cluster (red lines), for a cluster with $N = 100$ tracers (blue dashed curves), and for lensing only (green dash-dotted curves).

The black vertical lines indicate the GR expectation ($Y_1 = Y_2 = 0$).

files from CFHTLenS of 58 clusters at redshift $0.1 < z < 1.2$. A much more stringent constraint has been found by Salzano et al. (2017a) who however worked on a quite different class of models where the potential Φ and Ψ are modified in terms of one single free parameter $Y_1 \equiv Y_2 = \mathcal{Y}$ (although is still true that $\Phi \neq \Psi$). By combining X-ray mass profiles and strong+weak lensing analyses for 18 clusters studied within the CLASH collaboration, they found a very tight upper limit of $\mathcal{Y} \lesssim 0.16$ at 2σ .

For the general case $Y_1 \neq Y_2$, our simplified approach shows that the parameter Y_2 can be constrained at a level of 30–40% with a single cluster, down to $\sim 10\%$ for the combination of 20 clusters. However, the constraints on Y_1 are still one order of magnitude larger than what is found by other astrophysical probes. By focusing on the same class of theories as in Salzano et al. (2017a), we forecast $\mathcal{Y} \lesssim 0.26$ at 95% C.L. from the analysis of a single halo. In view of the above results, we remark the following:

- Our forecasts are obtained by assuming an ideal situation with perfect control of systematics for both lensing and internal kinematics analyses.

- The uncertainties considered here are reliable, given the current available data-sets, but slightly optimistic. Indeed, high-precision spectroscopic measurements for ~ 600 cluster members could be obtained only for a small fraction of observed galaxy clusters. Therefore, we consider a more realistic situation of ~ 100 tracers in the MG-MAMPOST fit. The results are listed in the seventh and eighth column of Table

N_h clusters	Vainshtein screening						$f(\mathcal{R})$ gravity		
	$N = 600$ (MAM)	$N = 600$ (lens)		$N = 600$ (joint)		$N = 100$ (joint)		$N = 600$	$N = 100$
	Y_1	Y_1	Y_2	Y_1	Y_2	Y_1	Y_2	$ f_{\mathcal{R}0} $	$ f_{\mathcal{R}0} $
1	$\lesssim 6.92$	$\lesssim 7.45$	$-0.72^{+1.55}_{-4.18}$	$\lesssim 2.75$	$0.08^{+0.32}_{-0.28}$	$\lesssim 3.56$	$0.10^{+0.44}_{-0.40}$	–	–
5	$\lesssim 4.10$	$\lesssim 3.62$	$0.04^{+0.52}_{-1.05}$	$\lesssim 1.65$	$0.06^{+0.20}_{-0.18}$	$\lesssim 1.87$	$-0.08^{+0.31}_{-0.20}$	$\lesssim 3.37 \times 10^{-5}$	$\lesssim 5.13 \times 10^{-5}$
10	$3.52^{+0.62}_{-3.99}$	$\lesssim 2.90$	$0.04^{+0.42}_{-0.63}$	$\lesssim 1.24$	$-0.05^{+0.17}_{-0.13}$	$\lesssim 1.65$	$0.01^{+0.24}_{-0.17}$	$\lesssim 1.12 \times 10^{-5}$	$\lesssim 3.24 \times 10^{-5}$
15	$3.18^{+0.70}_{-3.64}$	$\lesssim 2.44$	$0.07^{+0.49}_{-0.38}$	$0.04^{+1.00}_{-0.39}$	$0.01^{+0.12}_{-0.09}$	$\lesssim 1.20$	$-0.01^{+0.19}_{-0.16}$	$\lesssim 9.51 \times 10^{-6}$	$\lesssim 2.43 \times 10^{-5}$
20	$3.17^{+0.69}_{-3.61}$	$\lesssim 2.22$	0.07 ± 0.38	$0.08^{+0.77}_{-0.34}$	$0.01^{+0.09}_{-0.08}$	$\lesssim 1.02$	$0.01^{+0.16}_{-0.14}$	$\lesssim 7.11 \times 10^{-6}$	$\lesssim 1.79 \times 10^{-5}$

Table 3. Constraints at 95% C.L. forecasted from the MG-MAMPOSSt method with additional lensing information for the parameters of the two modified gravity models presented in this paper, in the case of clusters with $r_{200} = 2.0$ Mpc and $r_s = 0.3$ Mpc ($c \approx 6.67$). From column two to column eight: Vainshtein screening. Column nine and ten: chameleon $f(\mathcal{R})$ gravity. For both models we show the results when using ~ 600 and ~ 100 cluster members in the MG-MAMPOSSt fit.

3. As expected, in this case the constraints are $\sim 25\%$ weaker, but still good for Y_2 even for a single halo, confirming that the availability of lensing information plays a crucial role in the MG-MAMPOSSt analysis.

- The test carried out shows that galaxy cluster mass profiles are not able to provide tight constraints for the Newtonian potential Φ for VS (related to the coupling Y_1), compared to current astrophysical constraints, although the method offers a complementary test for these models at cosmological scales. Nevertheless, the combination of dynamics+lensing analyses in clusters promises to provide very useful information on the parameter Y_2 in VS models, for which the only constraint obtained at cosmological level is that of Sakstein et al. (2016). Indeed, the effective lensing mass, Eq. (15), for a NFW density profile reads as,

$$M_{\text{lens}} = M_{\text{NFW}} + \frac{r^2 M_{200} [Y_1(r_s - r) - 5Y_2(r_s + r)]}{8[\ln(1+c) - c/(1+c)]} \frac{1}{(r_s + r)^3}$$

$$\equiv M_{\text{dyn}} + M_2, \quad (44)$$

with

$$M_2 = \frac{r^2 M_{200}}{8(r_s + r)^3} \frac{Y_1(r - r_s) - 5Y_2(r_s + r)}{[\ln(1+c) - c/(1+c)]}. \quad (45)$$

We can see that the contribution of Y_2 to departures from GR is five times stronger than Y_1 . Moreover, the last term in Eq. (44) is always different from zero for any finite r , as shown by the relative ratios of the lensing mass profile in Fig. 9. Thus, we expect that joint lensing and dynamics analyses can constrain much better Y_2 than Y_1 .

In this perspective, we further outline that:

- The method we used to reconstruct the parameters from the simulated lensing mass profile only accounts for weak lensing (mock) data. In general, high precision joint strong+weak lensing analyses - like those performed by Umetsu et al. (2016); Caminha et al. (2017) - can determine the mass profile down to the cluster core. The structure of Eq. (26) and Eq. (44) suggests that the knowledge of the inner shape of the profile provides significant information in breaking the degeneracy between the model parameters.

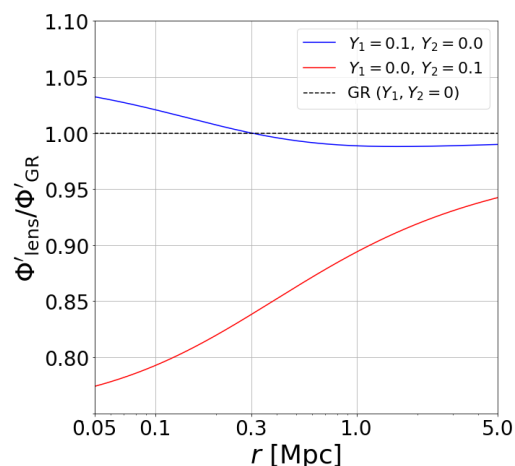


Figure 9. Ratios between the gradient of the lensing potential Φ'_{lens} and the gradient of GR gravitational potential Φ'_{GR} , obtained for a VS model with $Y_1 = 0.1, Y_2 = 0$ (blue) and $Y_1 = 0, Y_2 = 0.1$ (red). The NFW profile parameters are $r_{200} = 2.0$ Mpc and $r_s = 0.3$ Mpc.

5 Application II: chameleon screening

In this section, we present the MG-MAMPOSSt results for the sample of mock haloes assuming a fifth force mediated by a chameleon scalar field ϕ .

5.1 General chameleon screening

In the general case assuming that the interior solution for the scalar field is close to zero up to the screening radius, the magnitude of the additional force is totally determined by the background field value ϕ_∞ and the coupling constant \mathcal{Q} . We first analyse our sample of synthetic phase spaces in this framework, using Eq. (29) to model the chameleon profile and assuming $\phi_{\text{int}} \approx 0$. We perform a MCMC sampling of the likelihood from the internal cluster kinematics \mathcal{L}_{dyn} over the full parameter space ($\log r_s, \log r_{200}, \log \mathcal{A}_\infty, \phi_\infty, \mathcal{Q}$). For each parameter we assume flat priors in the allowed range, whose upper and lower bounds are listed in Table 2. Note that

for the GR kinematic parameters (r_s , r_{200} , \mathcal{A}_∞) we used the same values as in the VS case.

In principle, while the CS mechanism recovers GR at small scales, modifications of gravity are further Yukawa-suppressed for $r \gtrsim \lambda_\phi \equiv m_\phi^{-1} \sim \left[Q \mathcal{R}_0 M_{\text{PC}} c_L^2 / \phi_\infty \right]^{-1/2}$, where λ_ϕ is the background interaction range of the force, \mathcal{R}_0 is the background Ricci scalar. In order to satisfy local test of gravity at Solar System scales, it has been shown that λ_ϕ should be of the order of few Mpc (see e.g. Wang et al. 2012). In this simple treatment we neglect the Yukawa suppression of the chameleon field as in the MG-MAMPOSS_T analysis we consider only galaxies lying within a projected radius $R \sim r_{200} \sim \mathcal{O}(\text{Mpc})$. However, since in the Jeans equation the integral of the velocity dispersion extends far beyond the viral radius, for large Q the motion of member galaxies could be affected by the contribution of the tails of the integral even if the cluster is totally screened (i.e. $S \simeq r_{200}$). In order to avoid this problem, we make a conservative assumption that the effect of the chameleon field is zero everywhere if $S > 1.5 r_{200}$. A complete solution of the field equation will be investigated elsewhere.

Since in CS the lensing mass profile is unaffected by the fifth force, the contribution of additional lensing information affects only the NFW mass profile parameters r_{200} , r_s . Thus, in this case we follow the simpler approach of Pizzuti et al. (2019) who considered a Gaussian distribution $P_{\text{lens}}(r_s, r_{200})$ combined with the MG-MAMPOSS_T likelihood. The additional distribution is assumed to be derived by an unbiased (lensing) reconstruction, i.e. it is centered on the true values of the cluster mass profile's parameter. The standard deviations are defined assuming the above average uncertainties from real lensing analyses: $\sigma_{r_{200}}/r_{200} = 0.1$ and $\sigma_{r_s}/r_s = 0.3$. As for the correlation, we assume $\rho = 0.5$, checking that our results show only negligible effects when varying ρ over a reasonable range of values. We thus resampled our parameter space over the joint (log) likelihood $\ln \mathcal{L}_{\text{dyn}}(r_s, r_{200}, \mathcal{A}_\infty, \phi_\infty, Q) + \ln P_{\text{lens}}(r_s, r_{200})$. For our reference analysis, as before, we consider a massive halo with $r_{200} = 2.0 \text{ Mpc}$, $r_s = 0.3 \text{ Mpc}$ and ~ 600 tracers in the MG-MAMPOSS_T fit. In order to explore the full parameter range, we have considered the rescaled variables used in e.g. Terukina et al. (2014); Wilcox et al. (2015)

$$Q_2 = \frac{Q}{1+Q}, \quad \phi_2 = 1 - \exp\left[\frac{-\phi_\infty}{(M_{\text{PC}} c_L^2 10^{-4})}\right], \quad (46)$$

which run in the interval $[0, 1)$.

The results of the MCMC run for the MG parameters are shown in the left and central plot of Fig. 10. These results are similar to Terukina et al. (2014); Wilcox et al. (2015), who performed joint lensing and X-ray analyses of 58 clusters and of the massive Coma cluster respectively. Due to the degeneracy between the modified gravity parameters and the mass profile parameters, all values of the coupling factor and of the fields are allowed by galaxy internal kinematics, except for a small region corresponding to $0.8 \lesssim Q_2 \lesssim 0.9$ and $\phi_2 \gtrsim 0.8$ (left plot of Fig. 10). When including the lensing information in the analysis, a considerable fraction of the parameter space can be excluded at 3σ , (central plot of Fig. 10).

For small coupling factors, all scalar field values are still allowed by the data, with the screening mechanism active at small ϕ_∞ (Eqs. 30, 31). As the screening radius also depends

on the coupling, at large Q_2 the CS becomes very efficient also for large field values. In the intermediate region, however, $\phi_2 \rightarrow 1$ is no more allowed if $Q_2 \gtrsim 0.4$ as the cluster will be only partially screened and the modification of gravity cannot be entirely suppressed. Already with a single cluster, the combination of MG-MAMPOSS_T with additional lensing distribution provide useful information to investigate this intermediate range of values.

Note that the excluded region found with MG-MAMPOSS_T+lensing is shifted towards larger Q_2 w.r.t. what found by Terukina et al. (2014); Wilcox et al. (2015). This is not surprising as X-ray analyses and Jeans equation analyses perceive the effect of gravity and the lack of dynamical equilibrium in different ways, despite their sensitivity to the same gravitational potential.

Our results illustrate that the MG-MAMPOSS_T procedure, together with strong+weak lensing analyses, is an interesting method to test CS models at cluster scales – with present and future observations, the combination of different sets of data and methodologies (i.e. X-ray mass profile determinations) can improve the constraints on the allowed region in the plane (Q_2, ϕ_2) and thus on the viability of those theories at cosmological level. As for VS models, we study how our results change when combining the information of several clusters, by performing a MCMC sampling of

$$\ln \mathcal{L}_{\text{joint}} = \ln \mathcal{L}_{\text{tot}}(r_s, r_{200}, \mathcal{A}_\infty, \phi_\infty, Q) + N_{\text{h}} \ln P_{\text{lens}}(r_s, r_{200}),$$

where N_{h} is the number of haloes considered in the stack and the expression of \mathcal{L}_{tot} is the same as Eq. (33). As shown in the right plot of Fig. 10, the analysis of 10 clusters produces an improvement of the constraints for $Q_2 \gtrsim 0.3$, tightening the allowed region in the parameter space.

Since only few clusters have 600 known redshifts, we also reduce the number of tracers to $N = 100$, and display the iso-probability contours in the left plot of Fig. 11 for the joint lensing+kinematic likelihoods. While the MG-MAMPOSS_T analysis alone is insufficient to provide any bounds in (Q_2, ϕ_2) , the joint lensing+internal kinematics contours are almost identical to the previous analysis with $N = 600$. This indicates that the constraining power is mostly related to the additional information provided by lensing on the mass profile parameters r_{200}, r_s , confirming what was previously found for linear $f(\mathcal{R})$ (Appendix A of Pizzuti et al. 2020).

Keeping fixed $P_{\text{lens}}(r_s, r_{200})$, we generate a new phase space considering only 50 tracers to push further this ideal exercise. As we can see in the right plot of Fig. 11, in this case the weakening of the constraints affects the joint lensing+internal kinematics distribution. Although useful information can still be extracted in this limiting situation (e.g. by considering several clusters and suitably combining the member galaxy dynamics with real lensing and X-ray data), it is worth to notice that we are neglecting all the systematic effects. Indeed, such a small number of galaxies for each cluster is insufficient to correctly track the underlying total gravitational potential – incompleteness of the member galaxies sample as well as the effect of interlopers (i.e. galaxies in the field of view which do not belong to the cluster) can produce a bias in dynamic mass estimation if not properly taken into account (see e.g. Mamon et al. 2013).

Whereas for the VS model implemented in MG-MAMPOSS_T the new degrees of freedom Y_1 and Y_2 are scale-

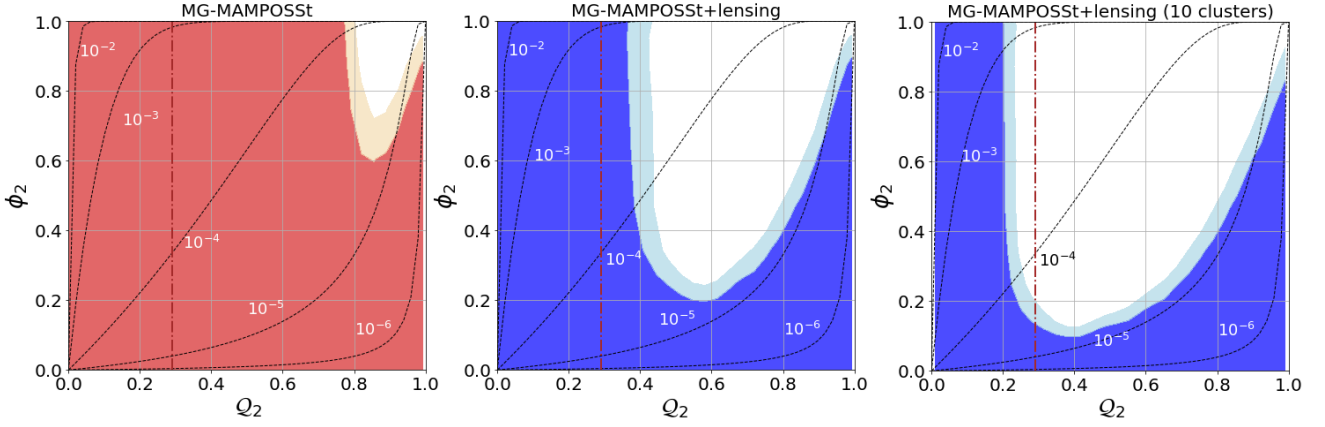


Figure 10. *Left and central panels:* results for the MCMC run in CS for one cluster in the sample. The shaded areas show the allowed regions in the plane of reduced coupling and scalar field, Eq. (46), ($Q_2 = Q/(1+Q)$, $\phi_2 = 1 - \exp[-\phi_\infty/(M_{\text{Pl}} c_l^2 10^{-4})]$) at 3σ (outer region) and 2σ (innermost region). *Left panel:* results from the MG-MAMPOSSt likelihood. *Central panel:* results from the joint lensing+internal kinematics analysis with $\sigma_{r_{200}}/r_{200} = 0.1$, $\sigma_{r_s}/r_s = 0.3$, $\rho = 0.5$ in the additional lensing distribution for the same cluster. In both plots 600 tracers are considered in the MG-MAMPOSSt fit. *Right panel:* joint lensing+internal kinematics for the combination of 10 clusters. In this and the following figures we use red-light red for MG-MAMPOSSt alone, blue-light blue for the joint lensing+internal kinematics. The black dashed curves indicate lines of constant ϕ/Q while the vertical brown dash-dotted lines correspond to the $f(R)$ value of the coupling $Q = 1/\sqrt{6}$.

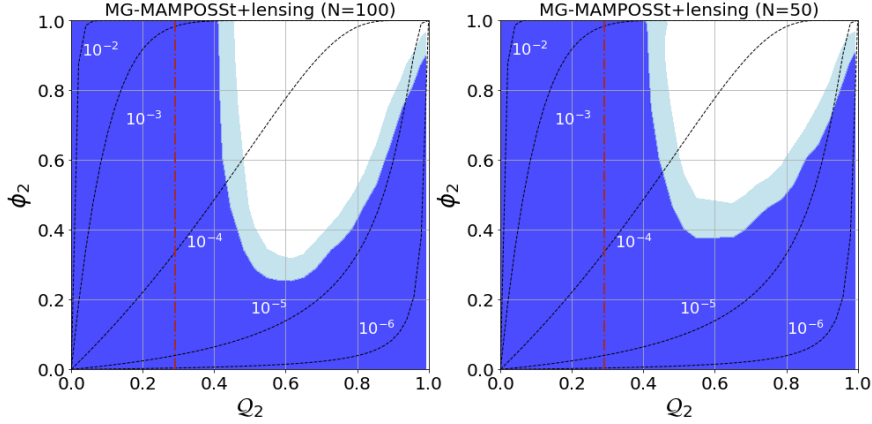


Figure 11. 3σ (outer region) and 2σ (innermost region) regions for the joint lensing+internal kinematic analysis of one cluster with $N = 100$ (left plot) and $N = 50$ (right plot) tracers considered in the MG-MAMPOSSt fit.

independent, this is no more true for CS models. The screening mechanism depends on the structure of the halo density profile, as shown by Eqs. (30), (31) – thus, the analysis of the member galaxy internal kinematics for clusters with different r_s , r_{200} should produce different constraints. For this reason, we consider four haloes generated with other combinations of r_s , r_{200} , in agreement with current observations, as discussed in Section 4.1. The new phase spaces are in two pairs characterised by concentrations $c = 4.2$ and $c = 3.3$ respectively, but obtained by changing r_s for one halo in the pair and r_{200} for the other halo with respect to the reference case $r_{200} = 2.0$ Mpc, $r_s = 0.3$ Mpc, $c = 6.67$. We apply again the MG-MAMPOSSt technique on phase spaces with ~ 600 particles within r_{200} drawn from those haloes – we derive the marginalized iso-probability contours for the modified gravity parameters, shown in Fig. 12. As expected, changing both r_s ,

r_{200} has an impact on the constrained allowed region, with the strongest constraint found for the highest value of the concentration and the smallest virial radius. Note that varying r_{200} produces a larger footprint on the bounds with respect to the change of r_s . This is not surprising, as the screening radius S depends on $\rho_s r_s^3 \propto r_{200}^3$ (Eq. 30).

5.2 $f(R)$ gravity

We now restrict to $f(R)$ gravity, a sub-class of chameleon theories where the coupling parameter is fixed to $Q = 1/\sqrt{6}$. Constraining this model translates into bounds on the background value of the scalaron field $|f_{R0}|$, which mediates the additional fifth force and it is related to ϕ_∞ as

$$\phi_\infty = -\sqrt{\frac{3}{2}} \ln(1 + f_{R0}) M_{\text{Pl}} c_l^2, \quad (47)$$

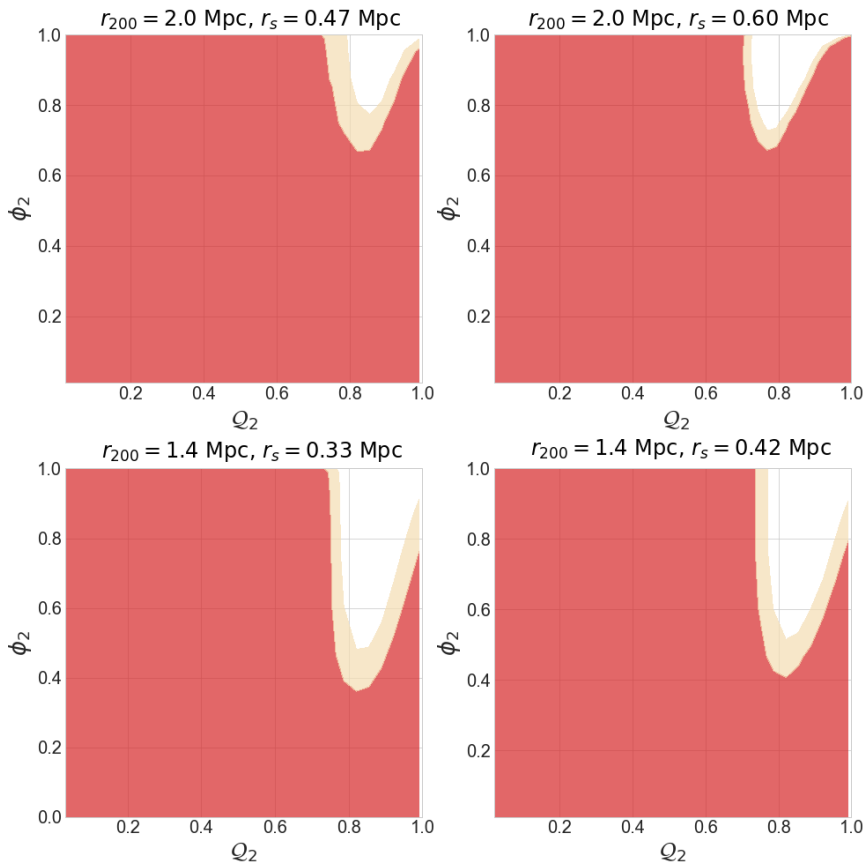


Figure 12. Result of the MG-MAMPOST analysis (internal kinematics only) for single haloes with different values of r_s and r_{200} with respect to the reference case. Color-codes is the same as previous plots. The left upper and left bottom plots refers to a concentration $c = 4.2$ obtained changing r_s and keeping fixed r_{200} (up) and vice-versa (bottom). The upper right and bottom right plots show the result for a concentration parameter $c = 3.3$.

according to Eq. (6).

For our reference analysis, we consider again a phase space of ~ 600 particles within r_{200} from an halo with $r_{200} = 2.0$ Mpc, $r_s = 0.3$ Mpc. In the lensing likelihood we adopt the same values of $\sigma_{r_{200}}$, σ_{r_s} and ρ as for our analysis in VS. We then vary the number of haloes considered in the MCMC run, the lensing standard deviations of r_{200} and r_s and the number of tracers in the internal kinematics analysis.

When considering a single halo, we found that ϕ_∞ is unconstrained at 95% C.L. in both cases of ~ 600 and ~ 100 tracers in projected phase space and for $\sigma_{r_{200}}/r_{200} = 0.1, 0.07$. This can be seen by looking at the central plot of Figure 10: when $Q = 1/\sqrt{6}$ (brown dash-dotted line) all values of ϕ_2 are allowed within 2σ . Moreover, changing the uncertainties σ_{r_s} in the lensing distribution produces a negligible effect on the joint likelihood. This is due to the degeneracy between r_{200} and the chameleon field, confirming what found in the simplified picture of linear $f(\mathcal{R})$ by Pizzuti et al. (2020). Indeed, if we fix the coupling constant $Q = 1/\sqrt{6}$, very large ϕ_∞ produces a maximum enhancement of the GR gravitational potential by a factor $1/3$ which can be compensated by slightly decreasing the overall radius of the halo. More in particular, a cluster with a smaller r_{200} in a strong modified $f(\mathcal{R})$ gravity ($\phi_\infty \gtrsim 10^{-4}$) produce the same effect of a cluster with a larger r_{200} in a GR scenario. In order to obtain a (weak)

bound on ϕ_∞ , the uncertainties on r_{200} in the lensing Gaussian should be reduced down to 5%. In this case we found $\phi_\infty \lesssim 9.52 \times 10^{-5}$ at 2σ , corresponding to $|f_{\mathcal{R}0}| \lesssim 7.77 \times 10^{-5}$.

As for the general CS model, we perform a stacked analysis to study the constraining power of our method in the ideal situation. In Fig. 13 we plot the marginalized likelihood obtained by Monte-Carlo sampling over a combined lensing+internal kinematics likelihood of 10 haloes. The black-dashed, blue and red lines indicate different values of $\sigma_{r_{200}}/r_{200}$ in the lensing Gaussian, 10% (black line) and 5% (red line). The uncertainties on r_s are fixed to 30% and the correlation to $\rho = 0.5$. The brown curve is obtained with 100 tracers considered in the MG-MAMPOST fit in each of the 10 haloes.

For $\sigma_{r_{200}} = 0.1 r_{200}$ and $\sigma_{r_{200}} = 0.05 r_{200}$ the combined distributions are almost identical, indicating that the information which can be obtained with our method for this particular model is already saturated with ~ 10 galaxy clusters. This extends the results in Appendix A of Pizzuti et al. (2020) to the case of chameleon $f(\mathcal{R})$ gravity. For the reference analysis ($\sigma_{r_{200}}/r_{200} = 0.1$ in the lensing distribution, black dotted line in of Fig. 13) and 10 haloes considered in the combined

likelihood we obtain (in terms of $f_{\mathcal{R}0}$):

$$|f_{\mathcal{R}0}| \leq 8.26 \times 10^{-6} \quad 1\sigma, \quad (48)$$

$$|f_{\mathcal{R}0}| \leq 1.12 \times 10^{-5} \quad 2\sigma. \quad (49)$$

When decreasing the number of tracers down to 100, the constraints become slightly weaker, $|f_{\mathcal{R}0}| \leq 3.24 \times 10^{-5}$ at 2σ , but still good if compared with the current cosmological constraints on $f(\mathcal{R})$. If the number of haloes in the combined likelihood is extended up to 20, the constraints improve to $|f_{\mathcal{R}0}| \leq 1.79 \times 10^{-5}$ and $|f_{\mathcal{R}0}| \leq 7.11 \times 10^{-6}$ at 2σ for 100 tracers and 600 tracers in the MG-MAMPOSSt fit, respectively. The results obtained varying the number of clusters considered in the analysis are listed in the last two columns of Table 3.

As mentioned before, the bounds can be substantially tightened by considering a less efficient screening mechanism, i.e. a smaller-size halo. The blue curve in Fig. 13 is obtained for 10 haloes with $r_{200} = 1.4$ Mpc and $r_s = 0.33$ Mpc. In this case, the upper limits become

$$|f_{\mathcal{R}0}| \leq 3.48 \times 10^{-6} \quad 1\sigma, \quad (50)$$

$$|f_{\mathcal{R}0}| \leq 5.40 \times 10^{-6} \quad 2\sigma. \quad (51)$$

The constraints further strengthen to $|f_{\mathcal{R}0}| \leq 3.56 \times 10^{-6}$ at 2σ in the case of 20 haloes. The bounds achieved by this simple exercise with a reasonable number of clusters are of the same order of magnitude of the results obtained from other cosmological probes (see e.g. Wilcox et al. 2015; Cataaneo et al. 2016; Jana & Mohanty 2019) for the specific class of $f(\mathcal{R})$ models. As already mentioned, it will be interesting to further evaluate the effect of X-ray analyses which could provide additional information to the dynamical parameters. We point out again that our results are obtained neglecting all systematics, as a proof of concept of the statistical power of the MG-MAMPOSSt method.

6 Summary and Conclusions

We have presented a new extension of the MG-MAMPOSSt code, aimed at constraining modified gravity models with the internal kinematics of the member galaxies in clusters. In particular, we have implemented two parametrisations for the Newtonian potential Φ , which governs the dynamics of member galaxies, based on Vainshtein screening and generic chameleon screening, both with NFW mass density profiles. These models cover the range of viable scalar-tensor theories after the recent measurement of the speed of gravitational waves. The code is based on the original MAMPOSSt method, developed by Mamon et al. (2013), which applies a Maximum Likelihood approach by solving the spherical Jeans equation in the projected phase space of member galaxies (R, v_z). As shown in Section 3, MG-MAMPOSSt can be used to fit together the mass and number density profile parameters, the velocity anisotropy parameter plus the additional degrees of freedom related to the modified gravity theory under study.

Under the assumptions of dynamical relaxation and spherical symmetry, we have illustrated the code's capabilities for a set of synthetic isolated dark matter haloes, generated by using the CLUSTERGEN code of Pizzuti et al. (2019). In this idealised setup, we have investigated

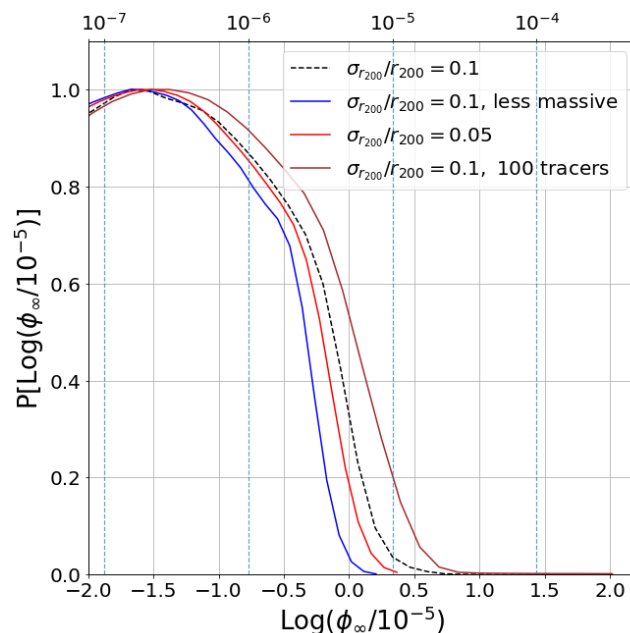


Figure 13. Marginalised distribution of the chameleon field in the case of $f(\mathcal{R})$ gravity ($Q = 1/\sqrt{6}$) obtained from the combined, joint lensing+internal kinematics likelihood for 10 clusters. In the lensing Gaussian we consider $\rho = 0.5$, $\sigma_{r_s} = 0.3 r_s$ and a variable $\sigma_{r_{200}}$. Black dotted line refers to the reference analysis with 600 tracers in MG-MAMPOSSt and $\sigma_{r_{200}}/r_{200} = 0.1$. The brown curve shows the case of 100 tracers while the blue distribution is for a phase space of 600 tracers but derived from a cluster with $r_{200} = 1.4$ Mpc and $r_s = 0.33$ Mpc. Finally, the red line refers to $\sigma_{r_{200}}/r_{200} = 0.05$. The dashed vertical lines indicate corresponding particular values of $|f_{\mathcal{R}0}|$.

the statistical degeneracy between the model parameters for VS and CS models that could obscure future realistic constraints in this context. We have further produced forecasts on those parameters in view of current and future observational surveys. The results are summarized as follows:

In the case of beyond Horndeski gravity we found that the resulting likelihood computed with MG-MAMPOSSt, based on the internal kinematics of member galaxies, exhibits a considerable degeneracy between the NFW parameters and the coupling constant Y_1 , which cannot be removed even when considering stacked haloes (see Figure 6 and the second column of Table 3). Additional information is required to break the degeneracy and constrain this class of modified gravity models.

Since for this family of models lensing is also affected as compared with GR, we simulated additional weak lensing information on the cluster's mass by considering a mock tangential shear profile with reliable uncertainties. We showed that the forecasted constraints obtained on the fifth force coupling Y_1 (associated to the Newtonian potential Φ) are of order unity, significantly weaker to other astrophysical probes. In particular, by considering 20 haloes' phase spaces with 600 tracers in the MG-MAMPOSSt fit, we obtain $Y_1 = 0.08^{+0.77}_{-0.34}$. When reducing the number of galaxies in each phase space to 100 the constraints weaken to $Y_1 \lesssim 1.02$. However, as we further showed, the joint internal kinemat-

ics+lensing analysis can be used to place tight constraints on the parameter Y_2 which appears in the relativistic potential Ψ and it has a stronger impact on the observed mass profile with respect to Y_1 . In this case, from the aforementioned analysis we found $Y_2 = 0.01^{+0.09}_{-0.08}$ and $Y_2 = 0.01^{+0.16}_{0.14}$ for 600 and 100 tracers in the fit respectively. The results are summarised in Figure 8 and in columns three to eight in Table 3. It is important to point out that galaxy cluster mass profiles provide a complementary, independent approach to test beyond Horndeski theories w.r.t astrophysical analyses, which relies on different physics and scales.

For CS, we have considered the general case with two free parameters, the fifth-force coupling strength Q and the background value of the scalar field ϕ_∞ . The MG-MAMPOSS_T code together with additional (lensing) information, provides useful insights on the allowed region of the parameter space, in terms of the re-scaled parameters $Q_2 = Q/(1+Q)$, $\phi_2 = 1 - \exp[-\phi_\infty/(M_{\text{Pl}} c^2 10^{-4})]$. We found that, given the dependence of the velocity dispersion on the gravitational potential, the module implemented in MG-MAMPOSS_T can be used to get complementary information to X-ray mass reconstructions, even if they are both sensitive to the Newtonian potential Φ .

In this class of models, lensing determinations are not affected by the fifth force, thus they can be used as a prior information on the cluster parameters r_s, r_{200} . Those priors have a strong impact on the constraining power of the method. Indeed, we found that decreasing the number of tracers from 600 to 100 in the MG-MAMPOSS_T fit but keeping the same simulated lensing distribution produces a negligible effect on the two dimensional iso-probability contours in the plane (Q_2, ϕ_2) , as shown in Figure 11.

For our reference analysis of a phase space with 600 galaxies and $\rho = 0.5$, $\sigma_{r_s} = 0.3 r_s$, $\sigma_{r_{200}} = 0.1 r_{200}$ in the lensing (Gaussian) distribution we found that the region corresponding to $0.45 \lesssim Q_2 \lesssim 0.7$ and $\phi_2 \gtrsim 0.6$ is excluded at more than 3σ . The combined likelihood of 10 haloes increases the range of the prohibited area up to $\phi_2 \gtrsim 0.3$ for values of Q_2 between 0.3 and 0.6.

The CS depends on the matter density perturbations, producing a stronger damping of the fifth force in more massive clusters. In Figure 12 we considered four different NFW haloes characterised by distinct values of r_s and r_{200} . We confirmed that smaller-size haloes provide better constraints due to a less-efficient screening mechanism. For clusters with $r_{200} = 1.4$ Mpc, the MG-MAMPOSS_T fit alone can exclude at 3σ the part of the parameter space where $\phi_2 \gtrsim 0.7$, $Q_2 \gtrsim 0.7$.

As a final step, we have focused on the specific sub-class of chameleon $f(\mathcal{R})$ gravity (i.e. $Q = 1/\sqrt{6}$, $\phi_\infty = -(3/2)^{1/2} \ln(1 + f_{\mathcal{R}0})$), in order to forecast the value of the background scalaron field. We obtain, for the reference case, $|f_{\mathcal{R}0}| \lesssim 1.12 \times 10^{-5}$ and $|f_{\mathcal{R}0}| \lesssim 7.11 \times 10^{-6}$ at 95% C.L. from the joint lensing+internal kinematics analysis of 10 clusters and 20 clusters, respectively. The bounds can be improved when using less massive clusters – in particular we found $|f_{\mathcal{R}0}| \leq 5.40 \times 10^{-6}$ and $|f_{\mathcal{R}0}| \leq 3.56 \times 10^{-6}$ for 10 and 20 haloes with $r_s = 0.33$ Mpc and $r_{200} = 1.4$ Mpc. The results are shown in Figure 13 and in the last two columns of Table 3.

In conclusion, MG-MAMPOSS_T offers a tool to probe GR and viable scalar-tensor theories at the scale of a galaxy clusters. A key aspect that has to be accounted for is the statistical degeneracy between the mass profile parameters and the MG parameters, at least for the models currently implemented in the code. This degeneracy is best broken by combining the three probes of galaxy clusters: kinematics, X-rays and lensing. Both ground-based (e.g. Vera C. Rubin Observatory) and space telescopes (e.g. Euclid), together with next generation spectrographs and X-ray observatories (e.g. the forthcoming Advanced Telescope for High-ENergy Astrophysics, Athena) will provide a large amount of high quality imaging and spectroscopic data for several galaxy clusters, allowing for a wide range of applications of our method.

In the future, we aim at extending the parametrisation of the gravitational potential to other mass density profiles, which would allow to investigate the interplay between the new degrees of freedom and the mass density profile parameters. It should be noted that it is not completely clear that the collapse of structures within all modified gravity theories studied here is accurately described by a NFW profile (see e.g. Corasaniti et al. 2020 and references therein).

The results presented here were obtained assuming the ideal conditions required by the limitations of our method. When dealing with real data, several systematics can affect the measurement producing spurious detection of modified gravity. For example, as shown in Pizzuti et al. (2020), the lack of dynamical relaxation and deviations from spherical symmetry have a relevant impact on the projected phase space and should be taken into account by adopting suitable selection criteria. The application of the MG-MAMPOSS_T method on the observed phase space of relaxed galaxy clusters will be performed in a forthcoming paper.

Data Availability

The data that support the findings of this study as well as the code described in the paper are available from the corresponding author, upon reasonable request. The code will be made publicly available in the future on GitHub at the following link https://github.com/Pizzuti92/MG-MAMPOSS_T.

Acknowledgements

The authors thank the referee Gary Mamon for his constructive criticism and comments which greatly improved the manuscript. LP acknowledges G. Paggi and M. Calabrese for useful comments and discussions. LP is partially supported by a 2019 "Research and Education" grant from Fondazione CRT. The OAVdA is managed by the "Fondazione Clément Fillietroz-ONLUS", which is supported by the Regional Government of the Aosta Valley, the Town Municipality of Nus and the "Unitedes Communes valdotaïnes Mont-Enfilus. I.D.S. has received support by the Czech Science Foundation GAČR (Project: 21-16583M), as well as through European Structural and Investment Funds and the Czech Ministry of Education, Youth and Sports (Project CoGraDS-CZ.02.1.01/0.0/0.0/15_003/0000437)

REFERENCES

- Amendola L., Kunz M., Saltas I. D., Sawicki I., 2018, *Phys. Rev. Lett.*, 120, 131101
- Amendola L., Bettoni D., Pinho A. M., Casas S., 2020, *Universe*, 6, 20
- Babichev E., Lehébel A., 2018, *JCAP*, 1812, 027
- Babichev E., Koyama K., Langlois D., Saito R., Sakstein J., 2016, *Class. Quant. Grav.*, 33, 235014
- Baker T., Bellini E., Ferreira P. G., Lagos M., Noller J., Sawicki I., 2017, *Phys. Rev. Lett.*, 119, 251301
- Barrow J. D., Cotsakis S., 1988, *Physics Letters B*, 214, 515
- Bartelmann M., 1996, *A&A*, 313, 697
- Ben Achour J., Crisostomi M., Koyama K., Langlois D., Noui K., Tasinato G., 2016, *JHEP*, 12, 100
- Binney J., Mamon G. A., 1982, *MNRAS*, 200, 361
- Biviano A., Salucci P., 2006, *A&A*, 452, 75
- Biviano A., et al., 2013, *A&A*, 558, A1
- Biviano A., et al., 2017, *A&A*, 607, A81
- Brok M., van de Ven G., Bosch R., Watkins L., 2013, *MNRAS*, 438
- Budzynski J. M., Kuposov S. E., McCarthy I. G., McGee S. L., Belokurov V., 2012, *MNRAS*, 423, 104
- Caminha G. B., et al., 2017, *A&A*, 607, A93
- Cataneo M., et al., 2015, *Phys. Rev. D*, 92
- Cataneo M., Rapetti D., Lombriser L., Li B., 2016, *JCAP*, 2016, 024–024
- Chen K.-F., Oguri M., Lin Y.-T., Miyazaki S., 2020, *ApJ*, 891, 139
- Corasaniti P. S., Giocoli C., Baldi M., 2020, *Phys. Rev. D*, 102, 043501
- Creminelli P., Vernizzi F., 2017, *Phys. Rev. Lett.*, 119, 251302
- Creminelli P., Lewandowski M., Tambalo G., Vernizzi F., 2018, *JCAP*, 1812, 025
- Crisostomi M., Koyama K., 2018, *Phys. Rev. D*, D97, 021301
- Crisostomi M., Lewandowski M., Vernizzi F., 2019, *Phys. Rev. D*, 100, 024025
- Dima A., Vernizzi F., 2018, *Phys. Rev. D*, D97, 101302
- Dutton A. A., Macciò A. V., 2014, *MNRAS*, 441, 3359–3374
- Ezquiaga J. M., Zumalacárregui M., 2017, *Phys. Rev. Lett.*, 119, 251304
- Falco M., Mamon G. A., Wojtak R., Hansen S. H., Gottlöber S., 2013, *MNRAS*, 436, 2639
- Ferraro S., Schmidt F., Hu W., 2011, *Phys. Rev. D*, 83, 063503
- Hoekstra H., 2003, *MNRAS*, 339, 1155
- Ishak M., 2019, *Living Rev. Rel.*, 22, 1
- Jain R. K., Kouvaris C., Nielsen N. G., 2016, *Phys. Rev. Lett.*, 116, 151103
- Jana S., Mohanty S., 2019, *Phys. Rev. D*, 99
- Kaiser N., Squires G., Broadhurst T., 1995, *ApJ*, 449, 460
- Kazantzidis S., Magorrian J., Moore B., 2004, *ApJ*, 601, 37–46
- Khoury J., 2013, *Class. Quantum Grav.*, 30, 214004
- Khoury J., Weltman A., 2004, *Phys. Rev. D*, 69
- Kobayashi T., 2019, *Rep. Prog. Phys.*, 82, 086901
- Kobayashi T., Hiramatsu T., 2018, *Phys. Rev. D*, D97, 104012
- Kobayashi T., Watanabe Y., Yamauchi D., 2015, *Phys. Rev. D*, D91, 064013
- Köhlinger F., Hoekstra H., Eriksen M., 2015, *MNRAS*, 453, 3107
- Koyama K., Sakstein J., 2015, *Phys. Rev. D*, 91, 124066
- Langlois D., 2019, *Int. J. Mod. Phys. D*, 28, 1942006
- Langlois D., Mancarella M., Noui K., Vernizzi F., 2017, *JCAP*, 1705, 033
- Laureijs R., et al., 2011, ArXiv e-prints, 1110.3193,
- Lewis A., Bridle S., 2002, *Phys. Rev. D*, 66
- Lombriser L., Koyama K., Zhao G.-B., Li B., 2012a, *Phys. Rev. D*, 85, 124054
- Lombriser L., Slosar A., Seljak U., Hu W., 2012b, *Phys. Rev. D*, D85, 124038
- Mamon G. A., Lokas E. L., 2005, *MNRAS*, 363, 705
- Mamon G. A., Biviano A., Murante G., 2010, *A&A*, 520, A30
- Mamon G. A., Biviano A., Boué G., 2013, *MNRAS*, 429, 3079
- Mamon G. A., Cava A., Biviano A., Moretti A., Poggianti B., Bettoni D., 2019, *A&A*, 631, A131
- Navarro J. F., Frenk C. S., White S. D. M., 1997, *ApJ*, 490, 493
- Old L., et al., 2015, *MNRAS*, 449, 1897
- Peirani S., et al., 2017, *MNRAS*, 472, 2153
- Pizzuti L., et al., 2016, *JCAP*, 1604, 023
- Pizzuti L., et al., 2017, *JCAP*, 1707, 023
- Pizzuti L., Saltas I. D., Casas S., Amendola L., Biviano A., 2019, *MNRAS*, 486, 596
- Pizzuti L., Sartoris B., Borgani S., Biviano A., 2020, *JCAP*, 04, 024
- Postman M., et al., 2012, *ApJS*, 199, 25
- Rapetti D., Allen S. W., Mantz A., Ebeling H., 2010, *MNRAS*, 406, 1796
- Rapetti D., Allen S. W., Mantz A., Ebeling H., 2011, *Prog. Theor. Phys., Suppl.*, 190, 179
- Read J. I., et al., 2021, *MNRAS*, 501, 978
- Rosati P., et al., 2014, *The Messenger*, 158, 48
- Sakstein J., 2013, *Phys. Rev. D*, 88, 124013
- Sakstein J., 2015a, *Phys. Rev. Lett.*, 115, 201101
- Sakstein J., 2015b, *Phys. Rev. D*, D92, 124045
- Sakstein J., 2018, *Int. J. Mod. Phys.*, D27, 1848008
- Sakstein J., Jain B., 2017, *Phys. Rev. Lett.*, 119, 251303
- Sakstein J., Wilcox H., Bacon D., Koyama K., Nichol R. C., 2016, *JCAP*, 1607, 019
- Saltas I. D., Lopes I., 2019, *Phys. Rev. Lett.*, 123, 091103
- Saltas I. D., Sawicki I., Lopes I., 2018, *JCAP*, 1805, 028
- Salzano V., Mota D. F., Dabrowski M. P., Capozziello S., 2016, *JCAP*, 1610, 033
- Salzano V., Mota D. F., Capozziello S., Donahue M., 2017a, *Phys. Rev. D*, 95
- Salzano V., Mota D. F., Capozziello S., Donahue M., 2017b, *Phys. Rev. D*, D95, 044038
- Schmidt F., Vikhlinin A., Hu W., 2009, *Phys. Rev. D*, 80, 083505
- Terukina A., Yamamoto K., 2012, *Phys. Rev. D*, 86, 103503
- Terukina A., Lombriser L., Yamamoto K., Bacon D., Koyama K., Nichol R. C., 2014, *JCAP*, 1404, 013
- Tiret O., Combes F., Angus G. W., Famaey B., Zhao H. S., 2007, *A&A*, 476, L1
- Umetsu K., 2020, *A&AR*, 28
- Umetsu K., Broadhurst T., Zitrin A., Medezinski E., Coe D., Postman M., 2011, *ApJ*, 738, 41
- Umetsu K., et al., 2012, *ApJ*, 755, 56
- Umetsu K., et al., 2014, *ApJ*, 795, 163
- Umetsu K., Zitrin A., Gruen D., Merten J., Donahue M., Postman M., 2016, *ApJ*, 821, 116
- Vasiliev E., 2019, Agama reference documentation ([arXiv:1802.08255](https://arxiv.org/abs/1802.08255))
- Wang J., Hui L., Khoury J., 2012, *Phys. Rev. Lett.*, 109, 241301
- Wilcox H., et al., 2015, *MNRAS*, 452, 1171
- Wilcox H., Nichol R. C., Zhao G.-B., Bacon D., Koyama K., Romer A. K., 2016, *MNRAS*, 462, 715
- Zitrin A., et al., 2015, *ApJ*, 801, 44
- Zumalacárregui M., García-Bellido J., 2014, *Phys. Rev. D*, D89, 064046

This paper has been typeset from a $\text{\TeX}/\text{\LaTeX}$ file prepared by the author.